

The GALEX Ultraviolet Virgo Cluster Survey (GUViCS). VII.: BCG UV upturn and the FUV-NUV color up to redshift 0.35[★]

S. Boissier¹, O. Cucciati², A. Boselli¹, S. Mei^{3,4,5}, and L. Ferrarese⁶

¹ Aix Marseille Univ, CNRS, LAM, Laboratoire d’Astrophysique de Marseille, Marseille, France
(e-mail: samuel.boissier@lam.fr)

² INAF - Osservatorio Astronomico di Bologna, via Gobetti 93/3, 40129 Bologna, Italy

³ LERMA, Observatoire de Paris, PSL Research University, CNRS, Sorbonne Universités, UPMC Univ. Paris 06, F-75014 Paris, France

⁴ Université Paris Denis Diderot, Université Paris Sorbonne Cité, 75205 Paris Cedex 13, France

⁵ Jet Propulsion Laboratory, California Institute of Technology, Cahill Center for Astronomy & Astrophysics, Pasadena, California, USA

⁶ National Research Council of Canada, Herzberg Astronomy and Astrophysics Program, 5071 West Saanich Road, Victoria, BC, V9E 2E7, Canada

2017

ABSTRACT

Context. At low redshift, early-type galaxies often exhibit a rising flux with decreasing wavelength in the 1000–2500 Å range, called “UV upturn”. The origin of this phenomenon is debated, and its evolution with redshift is poorly constrained. The observed GALEX FUV-NUV color can be used to probe the UV upturn approximately to redshift 0.5.

Aims. We provide constraints on the existence of the UV upturn up to redshift ~ 0.4 in the brightest cluster galaxies (BCG) located behind the Virgo cluster, using data from the GUViCS survey.

Methods. We estimate the GALEX far-UV (FUV) and near-UV (NUV) observed magnitudes for BCGs from the maxBCG catalog in the GUViCS fields. We increase the number of nonlocal galaxies identified as BCGs with GALEX photometry from a few tens of galaxies to 166 (64 when restricting this sample to relatively small error bars). We also estimate a central color within a 20 arcsec aperture. By using the r -band luminosity from the maxBCG catalog, we can separate blue FUV-NUV due to recent star formation and candidate upturn cases. We use Lick indices to verify their similarity to redshift 0 upturn cases.

Results. We clearly detect a population of blue FUV-NUV BCGs in the redshift range 0.10–0.35, vastly improving the existing constraints at these epochs by increasing the number of galaxies studied, and by exploring a redshift range with no previous data (beyond 0.2), spanning one more Gyr in the past. These galaxies bring new constraints that can help distinguish between assumptions concerning the stellar populations causing the UV upturn phenomenon. The existence of a large number of UV upturns around redshift 0.25 favors the existence of a binary channel among the sources proposed in the literature.

Key words. ultraviolet:galaxies ; galaxies: ellipticals and lenticulars, cD; galaxies:stellar content

1. Introduction

Code (1969) presented for the first time evidence of an excess of far-ultraviolet (FUV) light in the bulge of M31. The International Ultraviolet Explorer (IUE) observations of Ellipticals allowed astronomers to characterize this as “UV upturn”, i.e., a rising flux with decreasing wavelengths from about 2500 Å to 1000 Å (e.g., Bertola et al. 1982). The UV upturn was found in the nearby universe in quiescent gas depleted ellipticals and has been associated to old stars (O’Connell 1999; Ferguson 1999). This feature has also been found in other old stellar systems such as M32 (Brown 2004) or open clusters (Buson et al. 2006; Buzzoni et al. 2012). Empirical work to find the actual source of the upturn included the analysis of color-magnitude diagrams (Brown et al. 1998), the detection of individual horizontal branch stars (Brown et al. 2000), or surface brightness fluctuations (Buzzoni & González-Lópezlira 2008).

Since the UV upturn is found in early-type galaxies characterized by old stellar populations, an effect of age can be expected. Observed correlations also suggest a role of metallicity (Faber 1983; Burstein et al. 1988). However, these results have been extensively discussed (see the conflicting results in Deharveng et al. 2002; Rich et al. 2005; Boselli et al. 2005; Donas et al. 2007).

The recent work on absorption indices revealing old and young populations by Le Cras et al. (2016) has showed that there is still a strong interest to understand the nature of UV upturn sources and their contribution to stellar populations as a whole. From the point of view of the evolution of galaxies and the role of the environment, it is important to understand the UV emission associated with old stellar populations in early-type galaxies and to determine whether it is related to the environment (see Boselli et al. 2014).

Hills (1971) suggested that the UV emission in M31 could be related to the presence of very hot stars. Renzini & Buzzoni (1986) discussed the possible candidates in the context of stellar population evolution. This included young stars, hot horizontal

[★] Tables 2 to 5 are available in electronic form at the CDS via anonymous ftp to cdsarc.u-strasbg.fr (130.79.128.5) or via <http://cdsweb.u-strasbg.fr/cgi-bin/qcat?J/A+A/>

branch stars, post-AGB stars, and binaries. Several theoretical works studied the UV emission of various types of stars during their advanced evolution phases (e.g., Greggio & Renzini 1990; Dorman et al. 1993, 1995; D’Cruz et al. 1996). These works showed that their UV output is very sensitive to small differences in the assumptions made. Greggio & Renzini (1990) suggested that stellar evolution theory alone could not provide the explanation of the UV upturn.

It is still generally believed that the UV upturn is related to extreme horizontal branch stars (Brown 2004, and references therein). These stars could be low mass helium burning stars having lost their hydrogen-rich envelope (e.g., Han et al. 2007, and references within). However, the precise stellar evolution producing hot low mass stars is still debated. Recent models include single-star evolution with both metal-poor and metal-rich populations (e.g., Park & Lee 1997; Yi et al. 1998) or models including the effect of binarity, with stars losing their hydrogen envelopes during binary interactions (Han et al. 2007).

The various models proposed for the UV upturn sources predict drastic differences concerning the evolution of galaxy colors with redshift. Renzini & Buzzoni (1986) and Greggio & Renzini (1990) already suggested that observations at a look-back time of a few Gyr should allow us to distinguish between possible sources. In the case of single-star origin, the UV upturn is expected to occur late because it is produced by evolved stars. If it is related to binaries, its apparition can be more progressive. Higher redshift observations are needed to distinguish these different evolutionary scenarios.

From the observational point of view, Rich et al. (2005) found little evolution up to redshift 0.2 in a sample of 172 red quiescent galaxies (not restricted to the most massive or to central clusters) obtained by cross-matching SDSS and GALEX results. Lee et al. (2005) and Ree et al. (2007) compared the observed FUV-V color of nearby ellipticals to the brightest ellipticals in 12 remote clusters up to redshift 0.2, and also compared this color to a few previous works (see Brown 2004) up to redshift 0.6. These results suggest that the FUV-V restframe color is bluer by about 0.8 mag around redshift 0.2 with respect to redshift 0, with a large dispersion at all redshifts. The color of the few galaxies at redshifts higher than 0.2 is close to the average color at lower redshifts. Donahue et al. (2010) presented the evolution of the FUV-R color with redshift in 11 brightest cluster galaxies (BCGs) in the redshift range 0.05–0.2, detected in FUV, with little evolution. Direct studies of the evolution of the UV upturn with redshift are still limited to small samples and include only a few tens of objects when limited to BCGs. Table 1 list the samples of early-type galaxies with FUV and near-ultraviolet (NUV) magnitudes from GALEX.

Several colors or other quantities have been used to detect and study the UV upturn. One of them is simply the FUV-NUV GALEX color that is easily accessible from GALEX data. It has been used by, e.g., Boselli et al. (2005); Donas et al. (2007); Loubser & Sánchez-Blázquez (2011). This color probes the slope of the UV spectrum, and can be used to this end up to moderate redshift. In Fig. 1 we show the spectrum of NGC1399, a Fornax elliptical with a strong UV upturn at redshift 0. We also show the spectrum shifted for a few redshifts, and the evolution of the corresponding FUV-NUV color as a function of redshift. The FUV (around 1500 Å) and NUV (around 2300 Å) filters from GALEX are also indicated, showing that the FUV-NUV color probes the UV slope. The FUV-NUV color can thus be an indicator of the presence of an upturn, and of the value of the slope of the spectrum. As a visual reference, we also show the evolution for a flat UV spectrum. Any upturn will be by defini-

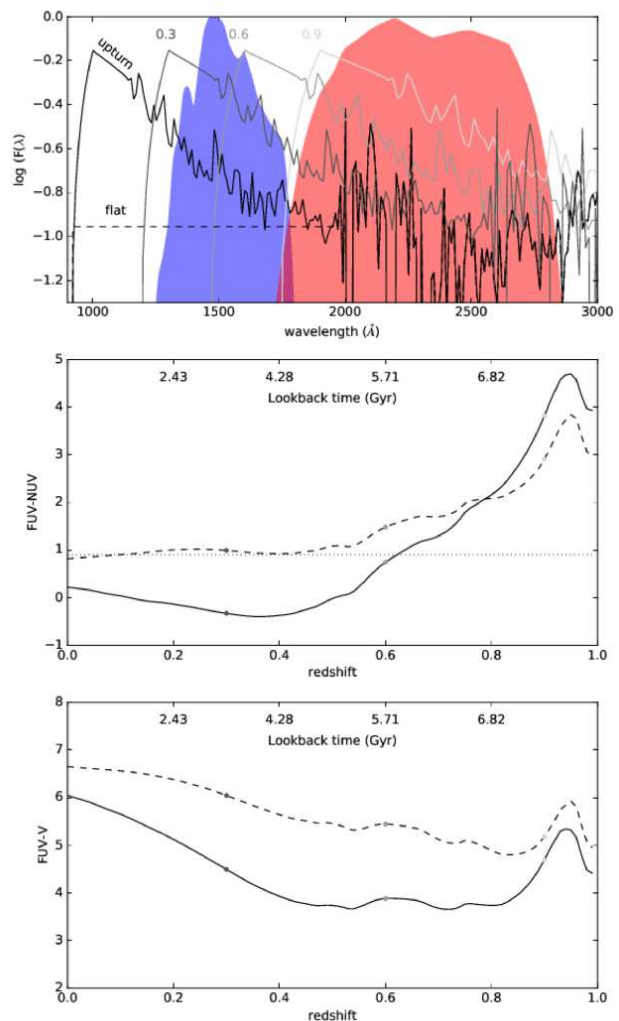


Fig. 1. Top: Arbitrarily scaled spectrum of NGC1399 (solid line). The spectrum was taken from the database of UV-Optical Spectra of Nearby Quiescent and Active Galaxies (<http://www.stsci.edu/science/sed/sed.htm>), the original UV data are from Burstein et al. (1988). The spectrum was smoothed for visualization, and extrapolated at low wavelength (between 912 and 1170 Å) to match a typical upturn galaxy spectra (Yi et al. 1998). This spectrum is also shown after redshifting to $z=0.3, 0.6, 0.9$. A “flat” version is also shown (i.e., removing the upturn) for reference purposes (see text in the introduction). The GALEX FUV and NUV passbands are respectively indicated as a blue and red shaded area. Middle: Evolution with redshift of the FUV-NUV color for the upturn and flat spectra as the solid and dashed curve, respectively. The dotted horizontal line corresponds to FUV-NUV=0.9, the limiting color for an upturn as defined by Yi et al. (2011). Bottom: Evolution with redshift of the FUV-V color of the upturn and flat spectra as the solid and dashed curve, respectively.

tion bluer than this reference (at redshift 0, it corresponds to a color close to the 0.9 limit, proposed by Yi et al. 2011, to characterize the presence of an upturn). On the contrary, old stellar populations without upturn are redder than this reference. The upturn FUV-NUV color is distinguishable from a flat spectrum up to approximately redshift 0.5. Beyond this redshift, no more flux is found in the observed FUV band, and the color can no longer be used to detect a UV upturn. The figure illustrates that the presence of a UV upturn can clearly be detected as a

Table 1. UV upturn in early-type galaxy FUV-NUV samples

Reference	redshift range	Galaxies	Statistics
Rich et al. (2005)	0-0.2	early types	172
Boselli et al. (2005)	0	Virgo early types	264
Boselli et al. (2014)	0	Virgo centrals	7
Ree et al. (2007)	0-0.2	BCGs	12
Donahue et al. (2010)	0.06-0.18	BCGs	10 ^a
Loubser et al. (2011)	0	BCGs	36
This work (all, FUV measurements)	0.05-0.35	BCGs	166
This work (best sample ^b)	0.05-0.35	BCGs	64
This work (confirmed upturn ^c)	0.05-0.35	BCGs	27

Notes. ^(a) Number of FUV detections. ^(b) Sample with low uncertainty on the central color (sum of uncertainties on each side lower than 1.2 mag) and excluding galaxies flagged as contaminated. ^(c) Red global NUV-*r* color and blue central FUV-NUV color (see Sect. 3.1).

observed FUV-NUV color at the redshifts considered in this paper (below redshift 0.4). In the nearby universe, the UV upturn is often studied on the basis of a color rather similar to FUV-V. Figure 1 shows differences between the flat and upturn cases that are similar to those for the FUV-NUV color. For this color, however, we find a greater evolution of the observed FUV-V color (in AB magnitudes) with redshift. This makes it impossible to adopt a single color threshold for the detection of an upturn over the same redshift range. The two bottom panels of this figure can still help the reader compare our study to this color choice. We note that this is very close to the classical $(1550-V)_{\text{Burstein}}$ from Burstein et al. (1988) with FUV-V (in the AB system) $\sim (1550-V)_{\text{Burstein}} + 2.78$ (Buzzoni et al. 2012).

The Virgo area was extensively studied in the FUV and NUV bands of GALEX in the context of the GUViCS project (Boselli et al. 2011). The photometry collected by GUViCS provides a deeper coverage than in most large areas over the sky. The UV properties of early-type galaxies inside the Virgo cluster were studied in Boselli et al. (2005). In the present paper, we take advantage of these data to extract FUV and NUV photometry for massive galaxies in the background of the cluster, up to a redshift of about 0.35.

We select a sample of BCG galaxies from the maxBCG catalog (Koester et al. 2007), extract FUV and NUV data for 177 of these galaxies from GUViCS, and perform a visual inspection to ensure the quality and noncontamination of these fluxes. Considering the small statistics of existing BCG samples with FUV data (e.g., only 36 galaxies in Loubser et al. 2011 at redshift 0; 12 in Rhee et al. 2007 up to redshift 0.2), even after removing the galaxies with possible contamination or large error bars, our sample brings new constraints for future models of the UV upturn population. We provide all our data in the form of easy-to-use tables for this purpose.

In Sect. 2, we present our sample and methods. The selection of galaxies showing upturn signs is discussed in Sect. 3. In Sect. 4, we show the dependences of the FUV-NUV color on luminosity and redshift in our sample, and discuss their implications. A summary is given in Sect. 5.

Throughout the paper, we use a flat cosmology ($H_0=70$, $\Omega_m=0.3$) to convert between look-back time τ and redshift (z). In our redshift range, the relation is linear with $\tau \sim 11.5 \times z$.

2. Samples and data

2.1. BCG sample

In order to obtain a sample of galaxies that are as evolved as possible in the background of the Virgo cluster area, we ex-

tracted a sample of BCGs using the maxBCG catalog that was computed from the Sloan Digital Sky Survey photometric data (Koester et al. 2007). We selected all galaxies with right ascension (RA) in the 180-195 degrees range and with declination (DEC) in the 0-20 degrees range, and with available GALEX images in the FUV and the NUV bands, from the GUViCS survey of this area (Boselli et al. 2011). This sample consists of 177 galaxies listed in Table 2. Koester et al. (2007) provided a number of properties of each BCG galaxy (position, redshift, luminosity) and of its cluster (e.g., number of members, luminosity of the members). We also performed a query to the DR13 SDSS release (Albareti et al. 2016) to obtain the latest spectroscopic information. We checked that the spectroscopic redshifts are in agreement with the Koester et al. (2007) values for the 71 galaxies for which it was provided, and we increased the number of spectroscopic redshifts in this way up to 150 objects, i.e., the vast majority of our sample. We also obtained the SDSS spectroscopic class (“GALAXY” for the 150 objects) and subclass based on line properties that result, in our sample, in one active galactic nucleus (AGN), three “BROAD-LINE” objects, one “STAR-FORMING” object. Finally, SDSS also provides measurements of the Mg2 and H β Lick indices often used in the literature to study the origin of the upturn in galaxies (e.g., Faber 1983; Burstein et al. 1988; Boselli et al. 2005; Buzzoni et al. 2012).

Table 2 compiles RA, DEC, photometric redshift, *r*- and *i*-band luminosity from the maxBCG catalog, while Table 3 provides the spectroscopic information obtained by querying the DR13 database: spectroscopic redshift, subclass, and Lick Mg2 and H β indices when available.

2.2. UV images

The early-type distant galaxies are often very faint in the ultraviolet bands, and a blind search can easily be affected by nearby objects (especially considering the ~ 5 arcsec resolution of GALEX) or low signal-to-noise ratio. Due to the nature of the GUViCS survey and the GALEX circular field of view, the survey is not homogeneous, and many galaxies were observed on several occurrences. We constructed stamps around the position of the BCGs by coadding any available UV images around our sources. This was done using the Montage software (Jacob et al. 2010) following the procedure described in Boissier et al. (2015), which allows the deepest possible UV exposure for each target. The UV original pixel is 1.5 arcsec wide, but since we reconstructed images from a variety of sources with arbitrary position shifts, we used Montage to project the UV im-

ages on a finer pixel grid. For practical reasons, we adopted the same pixel scale (0.187 arcsec per pixel) as the optical data that we obtained from the NGVS survey (Ferrarese et al. 2012), as discussed in Sect. 2.4.

2.3. UV photometry

Since we are targeting relatively small and faint galaxies whose shape in the UV is not known a priori, we computed photometry systematically in a number of circular rings around the BCG galaxies, with apertures of radii 20, 30, 50, 70, 90, 110, 130 pixels (with a size of 0.187 arcsecs), chosen to cover the range of sizes found in our sample. We note that the first aperture is only slightly larger than the GALEX PSF. We use it nevertheless because early-type galaxies are often very compact in the UV, and this allows us to have an estimate of the color even when a nearby galaxy could contaminate a larger aperture. The magnitude obtained is by definition partial. Aperture corrections for a point source at this size are 0.23 mag in both filters¹, thus the color is unchanged. This central aperture has the advantage that it often presents a higher S/N, and may be more sensible to UV upturn if the stellar populations giving rise to it are concentrated. NGC1399, which we use to illustrate a typical upturn as seen in the nearby universe, clearly shows a FUV-NUV color gradient in the inner 30 arcsec, with the maximum upturn at the center as can be seen in Fig. 3 of Gil de Paz et al. (2007). The UV spectrum shown in Fig. 1 was obtained in the IUE aperture. For our distant objects, we certainly probe a larger physical size, thus this NGC1399 reference is likely to be the bluest color we can expect for a galaxy with a central upturn.

The sky value was measured in many independent regions around the galaxy and is void of obvious sources. The photometry and associated uncertainties were then computed as in Gil de Paz et al. (2007). The photometry was corrected for the Galactic extinction, using the Schlegel et al. (1998) values for the visual extinction and $R_{FUV}=8.24$, $R_{NUV}=8.20$ (Wyder et al. 2007).

2.4. Optical images

For all these galaxies, we fetched optical images from the NGVS survey (Ferrarese et al. 2012). Because the UV area we started from is larger than the NGVS area, we obtained these observations for about half of our sample (84 out of 177 galaxies). For the others, we fetched SDSS images. The optical images are not crucial for the analysis in this work, but were used for visual inspection allowing for instance to flag for possible contamination by nearby galaxies, or signs of star formation in the form of spiral arms (Sect. 2.5) or other morphological peculiarities. In order to have homogeneous data; however, we use the SDSS photometry from the Koester et al. (2007) catalog for all our galaxies in the i and r band (in order to test the relations found in early-type galaxies and to test for the presence of a young stellar population). We do not perform photometry measurements in the optical images in this work.

2.5. Visual inspection

A visual inspection of our images was performed. This step was important for this work for several reasons:

- We identified four BCGs with strong signs of star formation (spiral arms, prominent and spread out UV emission) that would obviously pollute any signal from the UV upturn;
- We identified objects for which the UV photometry was polluted by a nearby companion. In optical images, it is easy to spot small companions that are unimportant in optical bands, but that can be the dominant source in the UV images if they are star-forming. Considering the GALEX PSF, in these cases the flux in the BCG region could be due to these companions and not to the BCG. Comparing the images, we can easily say when the UV emission is centered on a companion rather than on the BCG;
- We chose the best circular aperture for this work. Having measurements in a collection of apertures, we could see in the image the surface covered by each aperture. We then selected the best one according to the following rules: 1) if possible the aperture including all the emission observed in the UV image (when not possible, our magnitude was flagged as partial) and 2) in any case, an aperture not polluted by a nearby companion (when not the case, we used another flag to indicate contamination).

The inspection was performed independently by two people (O.C. and S.B.). A small discrepancy occurred for 25 % of the galaxies (in most of the cases a different optimal aperture was chosen with a different flag). The discrepancies were resolved through discussion (usually adopting the smaller aperture to avoid possible pollution by a companion).

Table 4 provides our results concerning the photometry, including the exposure time, the chosen aperture, the FUV and NUV magnitudes and their 1σ uncertainties. We have 11 galaxies without FUV measurements (measured flux below the sky level). In this case the table indicates a -99.9 magnitude and the -1σ column is replaced by the limiting magnitude as deduced from the sky noise measurement.

Table 5 provides the flags. For both FUV and NUV, a flag can be “ok” (the aperture encompasses all the observed emission in the image and there is no contamination), “part.” (we had to use a smaller aperture than the full observed emission to avoid contamination), or “contam.” (the flux is likely to be contaminated by a nearby source, usually a star-forming galaxy). When possible, we preferred to have a part. flag, with a meaningful color in a small aperture, but in some cases, it was impossible to avoid a contamination. We also added some notes that indicates clear signs of star formation and spiral arms (“spiral structure”), presence of arcs (“arc”), or presence of other signs that might be related to a merger or interactions (“shells/tails/asymmetric/mergers”). These flags allow the identification of objects that may be affected for example by a recent merger or by star formation. It may be useful to distinguish them since, e.g., Using GALEX imaging, Rampazzo et al. (2011) found signs of star formation in their sample of 40 nearby early-type galaxies in low density environments that can produce rings or arm-like structures. At high redshift (0.2 to 0.9), Donahue et al. (2015) found in their CLASH BCG sample that BCGs with star formation activity indeed show perturbed morphology, while quiet BCGs have a smooth aspect.

We found similar percentages of the various flags on the subsamples with deep NGVS or SDSS optical images. Our flags are thus not affected by the source of the optical image that was examined together with our UV images. The only exception is the arc flag. We visually recognized four arcs, all of them in the NGVS images. Deep high quality exposures are necessary to recognize this feature. In our figures, we identify the galaxies

¹ <http://www.galex.caltech.edu/researcher/techdoc-ch5.html>

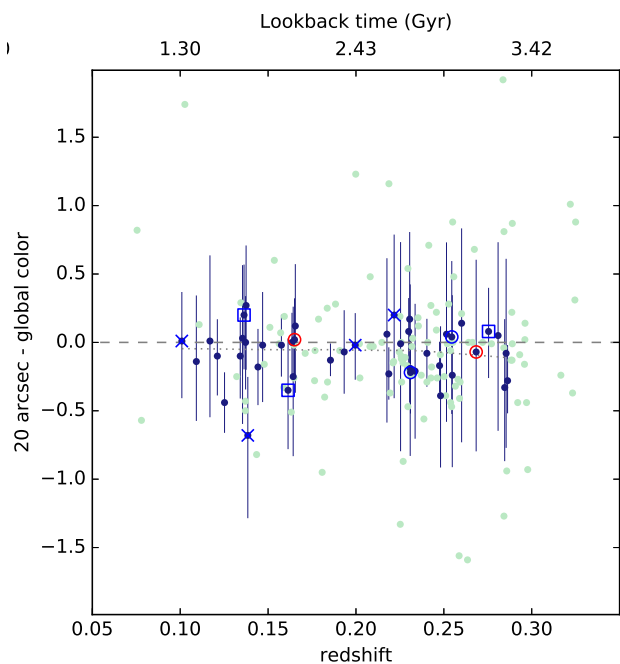


Fig. 2. Difference between the central and global FUV-NUV color. Galaxies with contamination or very large error bars (1σ interval on the central or global color larger than 1.2 mag) are indicated by a pale green circle. The dark blue symbols with error bars are all our other points, including indications from the visual inspection results (see Table 4 and text for details). In blue: obvious spiral structure (crosses); arcs (circles); strong asymmetries, shells, tails, or signs of merger (squares). The red circles indicate galaxies with the SDSS spectral subclass BROADLINE. The dashed lines indicates 0 (no color gradient) and the dotted line is a LOWESS fit to the dark blue points.

flagged for these different categories so that it is possible to see if the one where they are found present differences in a systematic manner with respect to the global sample or not.

2.6. Aperture issues

We also provide in Table 4 the central color, i.e., the color of the innermost aperture. It provides an idea of the central upturn in the case of an extended object, where the population responsible for the upturn might be more concentrated (see Sect. 2.3). When it was not possible to measure a FUV-NUV color in this aperture, the table indicates -99.9 color. We found that the central color correlates quite well with the total color. Figure 2 shows the difference between the central and global color as a function of redshift. Over the range of redshift considered, for an intrinsic constant size, the observed size may change by a factor of about 2 with redshift. The difference in the selected optimal size compensates for this effect. For galaxies with ok flags, we selected mostly the 30- or 50-pixel apertures. We chose 50 pixels for most of the nearby galaxies ($z < 0.15$), and 30 pixels for all the distant ones ($z > 0.25$). Figure 2 shows that we do not introduce a color trend by adopting the central color with respect to the global one. The central color has in general smaller error bars than the global color. The uncertainty is on average reduced by a factor of 3 when using the 20 arcsec aperture with respect to the total aperture. For this reason, in the following we perform an analysis of the UV upturn in this smallest aperture. This has two main advantages. First, by definition, our color does not correspond to the total galaxy, but when we can have a total galaxy,

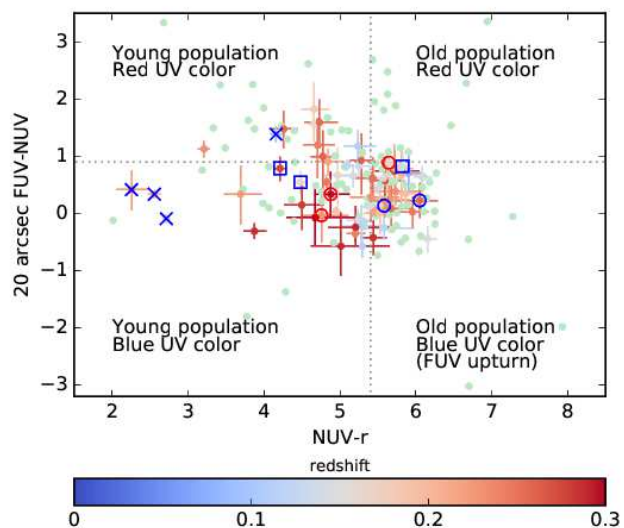


Fig. 3. Central FUV-NUV vs. global NUV- r color-color diagram in the best sample (colored by redshift). For comparison, pale green dots show the location of the other BCGs. The vertical line indicates NUV- r =5.4, above which there should be no contamination from young stars, and the horizontal line indicates FUV-NUV=0.9, below which the UV slope is consistent with a UV upturn (Yi et al. 2011). Peculiarities found in our visual inspection (blue) or in the SDSS spectral subclass (red) are marked as in Fig. 2.

they correlate. We are thus not limited to galaxies without contamination in the outer part (i.e., we can use galaxies having only a partial magnitude). Second, the error bar is smaller, which allows us to better distinguish trends. For the same adopted limit on the error bar size, we obtain larger statistics. Of course, this is not adequate for all analysis, thus Table 5 also provides the total magnitude measured as described above.

This allows us to obtain what we call the “best sample”, i.e., 64 BCGs with a central FUV-NUV color with global uncertainty (sum of the error bars on each side) lower than 1.2 magnitudes, and not contaminated.

2.7. Sample of local galaxies in GUViCS

A previous work on UV upturn in elliptical galaxies inside the Virgo cluster, based on GALEX data, was performed by Boselli et al. (2005). We refer the reader to this work for a detailed analysis of local galaxies. We consider here a similar comparison sample of local galaxies in the Virgo cluster, using the most recent set of data (Boselli et al. 2014). For all galaxies, the UV data have been taken from the GUViCS catalog of UV sources published in Voyer et al. (2014). The optical data in the SDSS photometric bands (Abazajian et al. 2009) have been taken, in order of preference, from the SDSS imaging of the *Herschel* Reference Survey (Boselli et al. 2010), published in Cortese et al. (2012), or from Consolandi et al. (2016). Given the extended nature of all these nearby sources, all magnitudes have been taken from imaging photometry of extended sources and thus are total magnitudes.

Among this sample, we identify the seven galaxies being central to subgroups in Virgo (Boselli et al. 2014) that are probably more similar to our BCGs than the other early-type galaxies in the local sample.

3. Confirmed upturn sample

3.1. Using optical photometry to exclude recent star formation

Brightest cluster galaxies are not systematically quiescent systems: 10 % to 30 % of BCGs in optically selected samples show star formation or AGN activity (Donahue et al. 2015, and references therein). A blue FUV-NUV is thus not necessarily the result of an evolved upturn population and can be the result of star formation activity. BCGs with star formation tend to have morphological signs such as filaments, elongated clumps, or knots (Donahue et al. 2015). From our visual inspection, we have identified a few obvious cases that can be excluded when focusing on the upturn phenomenon. Fortunately, Yi et al. (2011) and Han et al. (2007) showed that combining the FUV-NUV and NUV- r (or FUV- r) colors allows the separation of upturns, compared to galaxies that are simply blue as a result of young populations. Donahue et al. (2010) also showed that UV-optical colors are sensitive to even modest amounts of recent star formation. We thus present in Fig. 3 a FUV-NUV versus NUV- r color diagram for our sample. The NUV- r color is sensitive to young populations even if it does not probe exactly the same rest-frame waveband at all redshifts: blue colors indicate the presence of young stellar populations. We adopt the qualitative limits of Yi et al. (2011) to confirm the detection of rising UV flux when FUV-NUV is lower than 0.9; and the detection of a young population component when NUV- r is bluer than 5.4 mag. The galaxies that were flagged for spiral structures all fall on the young population side of the NUV- r =5.4 limit, three of them being even among the bluest objects in our galaxies. The figure clearly shows that we have a number of BCGs in the best sample at all redshifts falling in the upturn/old stellar population part of this diagram. We consider that these 27 BCGs are likely to present a UV upturn.

Another possible contribution to blue FUV-NUV color would be the presence of an AGN. O’Connell (1999) however discusses the contribution of known bright nuclei in elliptical galaxies (M87, NGC4278). Only 10 % of the FUV luminosity is related to the nuclei. While it could affect the FUV-NUV color, this is marginal with respect to our observational uncertainties. Moreover, the subclass from SDSS indicates one AGN and a few BROADLINE objects in our sample. Only three of them pass our UV photometry criteria (uncertainties, noncontamination). These few objects do not distinguish themselves from the rest of our sample, as can be seen in the figures where we marked them. In summary, our results should not be affected by AGNs.

3.2. Spectroscopic confirmation

We show in Fig. 4 the SDSS Mg2 and $H\beta$ Lick indices of the “confirmed upturn” sample (and of the full sample for comparison). These features have been used in the context of UV upturn studies since Faber (1983) and Burstein et al. (1988). SDSS provides values for many of our galaxies and the majority of our upturn sample (24 out of 27). In local galaxies, a trend between the Mg2 index and the strength of the upturn was found, with stronger upturns in more metallic galaxies. With our sample of BCG galaxies, we probe only the most massive of the galaxies with respect to the local sample. We thus do not find a trend with the Mg2 index as in the redshift 0 sample from Boselli et al. (2005). Our confirmed upturn sample behaves as the local “centrals”. As can be expected from color evolution of Fig. 1, the BCGs are slightly bluer at higher redshift, but present similar

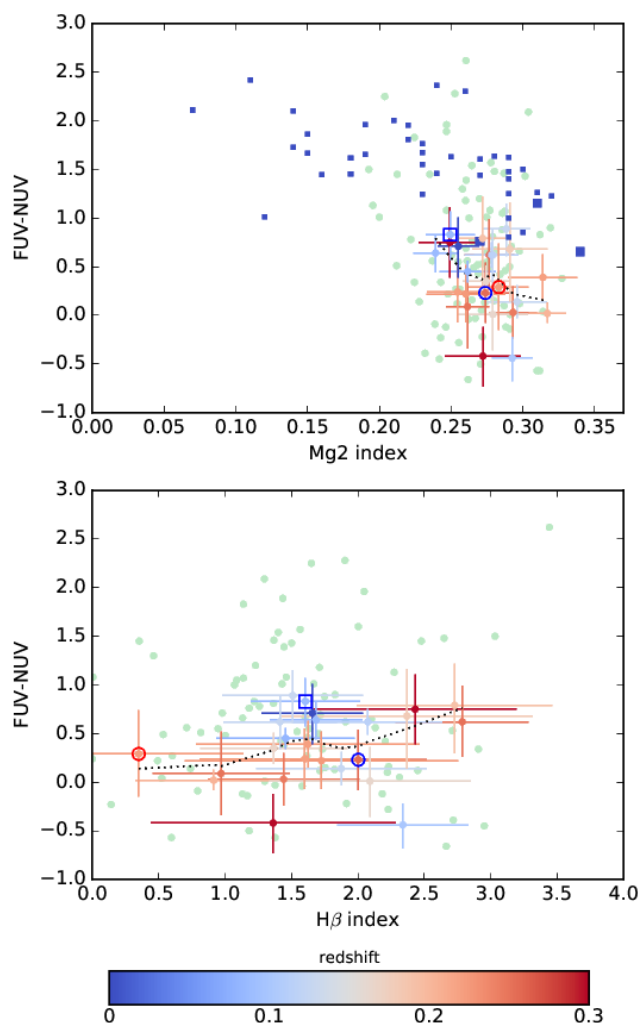


Fig. 4. FUV-NUV color as a function of the Mg2 and $H\beta$ Lick indices. Galaxies not pertaining to our upturn sample are shown as pale green dots. For the confirmed upturn galaxies, the symbols are colored according to their redshift. Peculiarities found in our visual inspection (blue) or in the SDSS spectral subclass (red) are marked as in Fig. 2. In the top panel, the squares show the relation found in the local sample (larger squares for centrals).

Mg2 values to the more massive of the local early-type galaxies showing upturns.

In the nearby universe, the $H\beta$ index has been used to distinguish galaxies with real upturn and those presenting residual star formation. The bottom panel of Fig. 4 shows its value for our full sample and confirmed upturns. We find a very mild trend of bluer UV colors for smaller $H\beta$ indices. This pattern is typical of upturns (Buzzoni et al. 2012). Blue UV colors related to star formation are instead found with higher values of the $H\beta$ index (above 2 \AA). Most of our BCGs are found with values between 1 and 2 \AA , typical of the passive galaxies with UV upturns.

From this section, we conclude that even if our selection of confirmed upturn were based on photometry alone, the spectroscopic information would confirm the status of these galaxies as quiescent with a real UV upturn, similar to that observed in the Local Universe and not polluted by residual star formation.

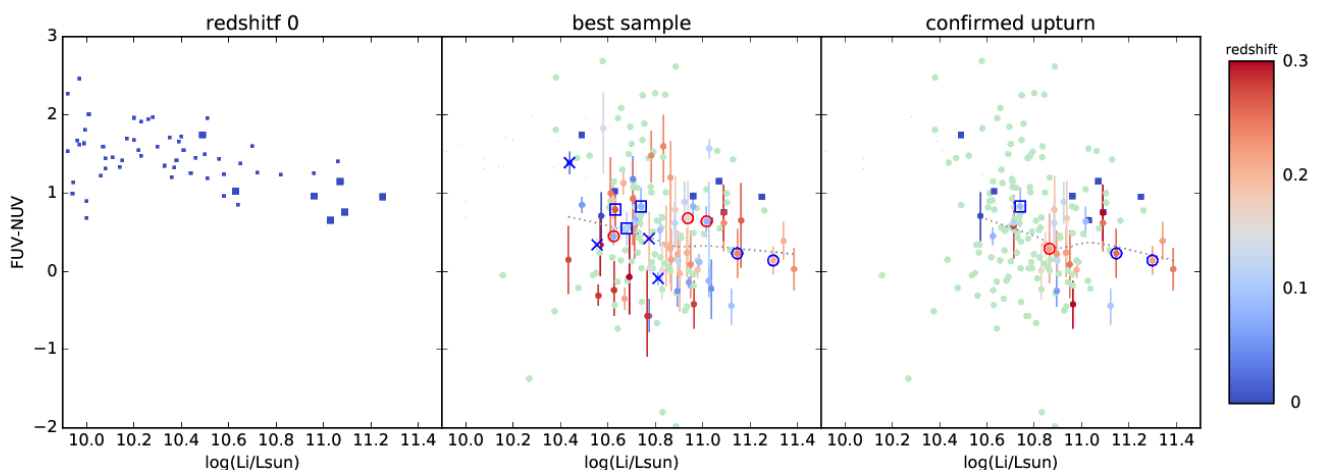


Fig. 5. FUV-NUV color as a function of the i -band luminosity. The left panel shows the relation for the redshift 0 early-type galaxies (Sect. 2.7). The central galaxies of the various subgroups in Virgo are indicated by larger symbols than the rest of the sample. These centrals are repeated in the other panels (squares). In the middle panel, we show our full and best sample (colored circles). We use the central FUV-NUV color (smaller error bar, larger statistics). Galaxies with contamination or very large error bars (1σ interval larger than 1.2 mag) are indicated by a pale green circle. For the other galaxies, the color corresponds to the redshift, as indicated in the color bar. Peculiarities found in our visual inspection (blue) or in the SDSS spectral subclass (red) are marked as in Fig. 2. The dotted line is a LOWESS fit to our sample. In the right panel, the colored circles are used only for the galaxies with confirmed upturn.

4. Results

4.1. FUV-NUV color vs. luminosity

We compare in Fig. 5 the FUV-NUV color and i -band luminosity of the local sample, our BCG sample, and the upturn sample. While some works have found an evolution with luminosity (Boselli et al. 2005), the color in our BCG sample varies little with luminosity. However, the sample covers a small range of i -band luminosity, since BCG have by definition higher masses (well traced by the i -band luminosity) than the general population of galaxies. The dispersion is reduced, however, when we restrict the sample to galaxies with confirmed upturn with a very mild trend.

The central galaxies in subgroups of Virgo are found in the same range of luminosities as our BCGs. In this range, the upturn sample is slightly bluer on average than the local sample, in agreement with the K-correction that can be deduced from Fig. 1. Loubser & Sánchez-Blázquez (2011) studied a sample of 36 nearby BCGs. Their FUV-NUV color (0.79 ± 0.055) is bluer than normal ellipticals of the same mass, but they do not find a strong dependence on mass or other parameters within BCGs. This is similar to what we find at higher redshift on average.

4.2. FUV-NUV color vs. redshift

As seen in the Introduction, the evolution with redshift of the UV upturn can bring direct constraints on the nature of stars producing it. Rich et al. (2005) did not find any evolution of the UV upturn up to redshift 0.2. Brown (2004) suggested that the UV upturn fades progressively with redshift up to redshift 0.6. Ree et al. (2007) compared the observed FUV-V color of nearby ellipticals to the ellipticals in 12 remote clusters up to redshift 0.2, and also compared this color to six objects in two clusters at redshifts around 0.3 and 0.5, suggesting a weak evolution of this color (they did not show the evolution of the FUV-NUV color, but provided the corresponding data in their table). Le Cras et al. (2016) has suggested that the UV upturn appears at redshift 1 in massive galaxies and becomes more frequent at lower redshift.

Their work is based on the fitting of line indices in synthesis population models where they can include a UV upturn component. They found that the rate of galaxies better fitted with models including an upturn is of 40 % at redshift 0.6 and 25 % at redshift 1. A weak evolution could be consistent with the binary model of Han et al. (2007), but the constraints are still scarce, and our sample can bring new information.

Figure 6 shows our measurement of the observed FUV-NUV color as a function of redshift for the BCG sample. Here, we use the best sample, i.e., all the galaxies with good constraints on the FUV-NUV color, which can be directly compared to published works with similar data. In the next section, we focus instead on the confirmed upturn that can be defined using optical photometry. Our galaxies are compared to the other samples of BCGs with published FUV-NUV colors: the 36 local BCGs of Loubser & Sánchez-Blázquez (2011) for which we indicate the average value and observed range of color, and at intermediate redshifts the BCG samples of Ree et al. (2007) and Donahue et al. (2010). Our sample adds new points at redshift lower than 0.2, and brings unique measurements in the redshifts 0.2 to 0.3, namely a significant increment in look-back time. When a FUV-NUV color could be measured with a global range of uncertainty lower than 1.2 magnitude (this is an arbitrary value that we chose in order to balance precision and statistics), we do obtain relatively blue colors. Most of these galaxies are bluer than the flat spectrum that we used as an artificial reference, as expected in the case of an upturn. A LOcally WEighted Scatterplot Smoothing (LOWESS) fit (implemented in Python by Cleveland 1979) performed on our BCGs combined with the two intermediate redshift samples stresses the trend of obtaining bluer colors at higher redshifts. However, this blue color is not necessarily a sign of a UV upturn, as discussed above. We thus study the FUV-NUV color as a function of redshift for confirmed upturn in the next section.

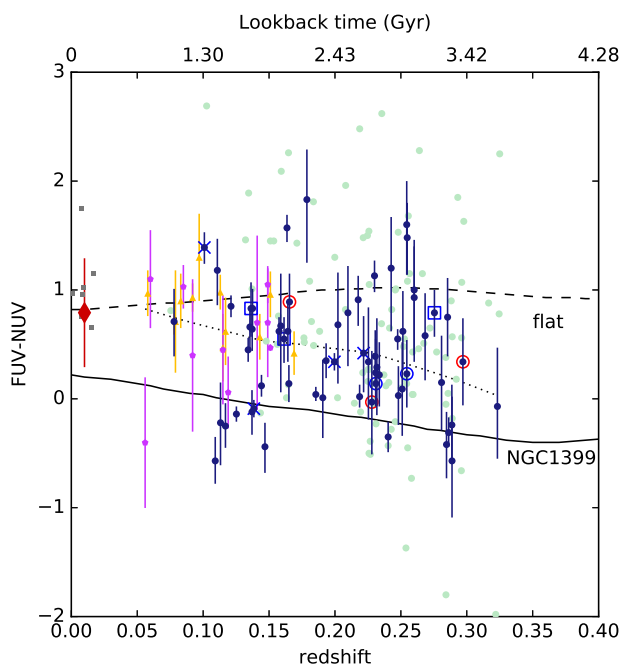


Fig. 6. Observed FUV-NUV color as a function of redshift. The gray squares are the redshift 0 centrals of Virgo subgroups (Sect. 2.7). The diamond is the average value of Loubser & Sánchez-Blázquez (2011), the error bar corresponding to the range of values they found for local BCGs. Intermediate redshift BCGs of Ree et al. (2007) and Donahue et al. (2010) are shown as orange triangles and magenta pentagons, respectively. The circles correspond to our sample for which we use the central FUV-NUV color (smaller error bar, larger statistics). Galaxies with contamination or very large error bars (1σ interval larger than 1.2 mag) are indicated by pale green circles, others by dark blue circles with corresponding error bars. Peculiarities are marked as in Fig. 2 (noted in our visual inspection in blue; noted in the SDSS spectral subclass in red). The solid (dashed) curve show the FUV-NUV color for the upturn spectrum of NGC1399 (for a flat spectrum) as a function of redshift. A LOWESS fit to our sample combined with the points of Donahue et al. (2010) and Ree et al. (2007) is indicated as the dotted line.

4.3. Detected UV upturn up to look-back times of 3.5 Gyr

In Fig. 7, we finally show the FUV-NUV color as a function of redshift for our BCGs, this time indicating only the BCGs for which a UV upturn is considered very likely based on the color-color diagram and the spectroscopic confirmation discussed in section 3.

We include in the figure the evolution predicted by different models. At all our redshifts, we selected very massive passive galaxies. It is likely that their stellar mass or i luminosity does not evolve much over the considered period since their star formation must have occurred at much earlier times in such galaxies (Thomas et al. 2005). The FUV-NUV evolution with redshift may thus be close to the actual color evolution of passively aging very massive galaxies. However, we cannot be sure that we select the precursors of redshift 0 upturn galaxies when we select upturns at higher redshift. Thus, the evolution with redshift that we present is not necessarily the redshift occurring in any individual galaxy. Even so, our results bring a new constraint for the stellar evolution models producing a UV upturn since models should at least predict the possibility of an upturn at the redshift when it is observed, which is not necessarily the case for all models.

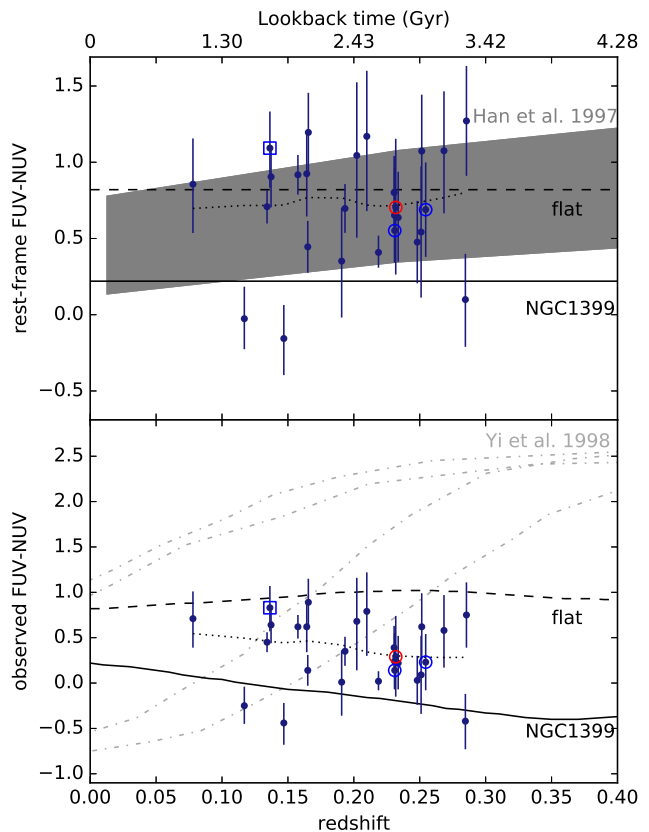


Fig. 7. FUV-NUV color as a function of redshift as in Fig. 6, but keeping only our BCG galaxies with old populations and UV upturn, as defined by the bottom right part of Fig. 3 (confirmed upturn sample). In the top panel, we show the rest-frame color. We corrected the observed points assuming the NGC1399 spectrum since we selected upturn galaxies. In the bottom panel we show the observed color. In each panel our points are compared to model predictions. The shaded area indicates the evolution of the rest-frame color for a SSP model of Han et al. (2007) including binaries (assuming a redshift 5 formation). The dot-dashed lines indicate the observed colors in typical models of Yi et al. (1998) based on single stars, for infall histories from Tantalo et al. (1996) for two galaxy masses (10^{12} and $5 \cdot 10^{11} M_{\odot}$), and two mass-loss efficiency parameter (0.7 for the two lower and 1 for the two upper curves). The dotted curve is a LOWESS fit to our data.

The rest-frame FUV-NUV colors for the SSP models of Han et al. (2007) are shown in the top panel. We computed rest-frame colors for our galaxies assuming the NGC1399 spectrum. In future model computations, it should be straightforward to obtain the observed color to compare it directly to the values provided in our tables to avoid this step. The weak evolution they propose is quite consistent with the lack of evolution found in our sample and the colors are globally consistent with these galaxies; we recall that they do not represent the full population of BCGs, but those presenting a UV upturn, which is a significant fraction (27 out of the 64 galaxies in the best sample).

We also show in the figure four typical models among those presented in Yi et al. (1998) for two infall accretion histories and for two values of their mass-loss efficiency parameters. We refer to their paper for a more detailed description of their models. In this case, we reproduce their prediction for the observed color $m(1500)-m(2500)$, which are not the GALEX bands but probe the UV slope in a similar wavelength range. These models tend

to be characterized by more ample and rapid variations than the Han et al. (2007) model is. Such large variation is not favored by our data (at least for a fraction of the BCG population).

We note that the models were basically constructed on the basis of redshift 0 constraints, with large uncertainties on the population responsible for the UV upturn. The inclusion of binary evolutions by Han et al. (2007) seems to help reproduce the observed upturn at look-back times of around 3 Gyr that we find in many of our galaxies.

Ciocca et al. (2017) recently found at redshift 1.4 blue color gradients in ellipticals in one cluster, with bluer UV-U colors in their center that may indicate the existence of a UV upturn population at even higher redshift.

4.4. Environment influence on the UV upturn?

We verified whether there is a correlation between the FUV-NUV color and other parameters in the maxBCG catalog. We could not find any significant trend, especially with those parameters related to the environment (e.g., number of cluster members). This is consistent with the findings of Yi et al. (2011) and Loubser & Sánchez-Blázquez (2011), suggesting that the UV upturn is intrinsic to galaxies and not directly related to their environment.

5. Conclusions

This work extends by a factor of several the size of BCG samples and provides constraints on their UV color. For the first time, we bring constraints on this subject to the redshift range 0.2–0.35, almost multiplying by 2 the look-back time with respect to previous studies.

We took advantage of the GUViCS survey to study the FUV-NUV color (probing the UV slope) of 177 massive galaxies of the maxBCG catalog. Even if it is poorly constrained for many of them (due to their intrinsic faintness, and low exposure time in part of the GUViCS survey), we measured the FUV magnitude for 166 objects in this sample. Removing from this sample the galaxies with relatively large uncertainties and those with contamination, we obtained an interesting constraint (sufficient to distinguish different models) on the (central) FUV-NUV color of 64 BCGs at redshift 0.05 to 0.35.

Our most important result is that 27 out of the 64 BCGs with good photometry at these redshifts present the characteristic of a UV upturn. They are selected on the basis of their blue FUV-NUV color, and of red optical colors suggesting an old underlying stellar population. The quiescent nature of these galaxies is confirmed by spectroscopic information. They bring important constraints for models of the stellar populations responsible for the UV upturn phenomenon in very massive early-type galaxies. The comparison of our new data set with models from the literature favors a mild evolution with redshift like that obtained by models taking into account the effect of binaries on stellar evolution (Han et al. 2007). In conclusion, our data favors the existence of a binary channel to produce very hot stars that can produce a UV upturn, even up to redshift 0.35. This empirical work cannot give a definitive answer, however. Our tabulated data should offer a new constraint for future models of stellar evolution.

From the empirical point of view, follow-up work could be done to increase the statistics on the basis of extensive UV and optical data sets. Especially, a search for all massive galaxies, ellipticals, and BCGs in the NGVS optical catalog, and a similar

systematic measurement of the UV color, but also of the UV-optical colors would be useful. In the long term, future large UV facilities (e.g., LUVOIR) could allow us to directly probe the UV spectrum of massive galaxies, providing more direct constraints on this still enigmatic phenomenon.

Acknowledgements. This research is based on observations made with the NASA Galaxy Evolution Explorer. GALEX is operated by NASA by the California Institute of Technology under NASA contract NAS5-98034. We wish to thank the GALEX Time Allocation Committee for the generous allocation of time devoted to GUViCS. This research made use of Montage, funded by the National Aeronautics and Space Administration's Earth Science Technology Office, Computation Technologies Project, under Cooperative Agreement Number NCC5-626 between NASA and the California Institute of Technology. Montage is maintained by the NASA/IPAC Infrared Science Archive.

References

- Abazajian, K. N., Adelman-McCarthy, J. K., Agüeros, M. A., et al. 2009, *ApJS*, 182, 543
- Albareti, F., Allende Prieto, C., Almeida, et al. 2016, arxiv:1608.02013
- Bertola, F., Capaccioli, M., & Oke, J. B. 1982, *ApJ*, 254, 494
- Boissier, S., Boselli, A., Voyer, E., et al. 2015, *A&A*, 579, A29
- Boselli, A., Boissier, S., Héinis, S., et al. 2011, *A&A*, 528, A107+
- Boselli, A., Cortese, L., Deharveng, J. M., et al. 2005, *ApJ*, 629, L29
- Boselli, A., Eales, S., Cortese, L., et al. 2010, *PASP*, 122, 261
- Boselli, A., Voyer, E., Boissier, S., et al. 2014, *A&A*, 570, A69
- Brown, T. M. 2004, *Ap&SS*, 291, 215
- Brown, T. M., Bowers, C. W., Kimble, R. A., Sweigart, A. V., & Ferguson, H. C. 2000, *ApJ*, 532, 308
- Brown, T. M., Ferguson, H. C., Stanford, S. A., & Deharveng, J.-M. 1998, *ApJ*, 504, 113
- Burstein, D., Bertola, F., Buson, L. M., Faber, S. M., & Lauer, T. R. 1988, *ApJ*, 328, 440
- Buson, L. M., Bertone, E., Buzzoni, A., & Carraro, G. 2006, *Baltic Astronomy*, 15, 49
- Buzzoni, A., Bertone, E., Carraro, G., & Buson, L. 2012, *ApJ*, 749, 35
- Buzzoni, A. & González-Lópezlira, R. A. 2008, *ApJ*, 686, 1007
- Ciocca, F., Saracco, P., Gargiulo, A., & De Propriis, R. 2017, *MNRAS*[arXiv:1701.02736]
- Cleveland, W. 1979, "Journal of the American Statistical Association 74", 368, "829
- Code, A. D. 1969, *PASP*, 81, 475
- Consolandi, G., Gavazzi, G., Fumagalli, M., Dotti, M., & Fossati, M. 2016, *A&A*, 591, A38
- Cortese, L., Boissier, S., Boselli, A., et al. 2012, *A&A*, 544, A101
- D'Cruz, N. L., Dorman, B., Rood, R. T., & O'Connell, R. W. 1996, *ApJ*, 466, 359
- Deharveng, J.-M., Boselli, A., & Donas, J. 2002, *A&A*, 393, 843
- Donahue, M., Bruch, S., Wang, E., et al. 2010, *ApJ*, 715, 881
- Donahue, M., Connor, T., Fogarty, K., et al. 2015, *ApJ*, 805, 177
- Donas, J., Deharveng, J.-M., Rich, R. M., et al. 2007, *ApJS*, 173, 597
- Dorman, B., O'Connell, R. W., & Rood, R. T. 1995, *ApJ*, 442, 105
- Dorman, B., Rood, R. T., & O'Connell, R. W. 1993, *ApJ*, 419, 596
- Faber, S. M. 1983, *Highlights of Astronomy*, 6, 165
- Ferguson, H. C. 1999, *Ap&SS*, 267, 263
- Ferrarese, L., Côté, P., Cuillandre, J.-C., et al. 2012, *ApJS*, 200, 4
- Gil de Paz, A., Boissier, S., Madore, B. F., et al. 2007, *ApJS*, 173, 185
- Greggio, L. & Renzini, A. 1990, *ApJ*, 364, 35
- Han, Z., Podsiadlowski, P., & Lynas-Gray, A. E. 2007, *MNRAS*, 380, 1098
- Hills, J. G. 1971, *A&A*, 12, 1
- Jacob, J. C., Katz, D. S., Berriman, G. B., et al. 2010, *Montage: An Astronomical Image Mosaicking Toolkit*, Astrophysics Source Code Library
- Koester, B. P., McKay, T. A., Annis, J., et al. 2007, *ApJ*, 660, 239
- Le Cras, C., Maraston, C., Thomas, D., & York, D. G. 2016, *MNRAS*, 461, 766
- Lee, Y.-W., Ree, C. H., Rich, R. M., et al. 2005, *ApJ*, 619, L103
- Loubser, S. I. & Sánchez-Blázquez, P. 2011, *MNRAS*, 410, 2679
- O'Connell, R. W. 1999, *ARA&A*, 37, 603
- Park, J.-H. & Lee, Y.-W. 1997, *ApJ*, 476, 28
- Rampazzo, R., Annibali, F., Marino, A., et al. 2011, *Ap&SS*, 335, 201
- Ree, C. H., Lee, Y.-W., Yi, S. K., et al. 2007, *ApJS*, 173, 607
- Renzini, A. & Buzzoni, A. 1986, in *Astrophysics and Space Science Library*, Vol. 122, *Spectral Evolution of Galaxies*, ed. C. Chiosi & A. Renzini, 195–231
- Rich, R. M., Salim, S., Brinchmann, J., et al. 2005, *ApJ*, 619, L107
- Schlegel, D. J., Finkbeiner, D. P., & Davis, M. 1998, *ApJ*, 500, 525
- Tantalo, R., Chiosi, C., Bressan, A., & Fagotto, F. 1996, *A&A*, 311, 361
- Thomas, D., Maraston, C., Bender, R., & Mendes de Oliveira, C. 2005, *ApJ*, 621, 673
- Voyer, E. N., Boselli, A., Boissier, S., et al. 2014, *A&A*, 569, A124
- Wyder, T. K., Martin, D. C., Schiminovich, D., et al. 2005, *ApJS*, 173, 293
- Yi, S., Demarque, P., & Oemler, Jr., A. 1998, *ApJ*, 492, 480
- Yi, S. K., Lee, J., Sheen, Y.-K., et al. 2011, *ApJS*, 195, 22

Table 2. BCG galaxies in our sample. They are selected from the reference catalog of Koester et al. (2007), from which we list here RA, DEC, photometric redshift, r and i band luminosities.

ID	RA (deg)	DEC (deg)	phot. redshift	L_r ($10^{10} L_{\odot}$)	L_i ($10^{10} L_{\odot}$)
BCG24	188.57278	9.766238	0.243050	17.90260	21.94700
BCG129	186.45179	7.971470	0.248450	9.48259	11.81850
BCG271	191.04632	14.482497	0.275450	11.28250	14.54510
BCG304	182.92986	8.018963	0.264650	18.48990	24.32040
BCG485	188.94962	15.555812	0.267350	7.44125	9.18799
BCG671	183.13768	6.076853	0.132350	8.40151	10.62250
BCG692	187.03522	8.945062	0.267350	16.49510	19.86410
BCG933	181.14637	11.095937	0.237650	11.01730	13.09370
BCG1076	188.90784	13.177456	0.261950	9.87069	12.29600
BCG1123	190.82471	19.013533	0.116150	9.03394	10.88040
BCG1140	184.92495	0.840782	0.299750	14.13630	18.22730
BCG1152	182.95640	8.439066	0.135050	7.61520	9.68125
BCG1187	183.29939	14.229333	0.299750	10.18440	12.66650
BCG1251	183.28358	12.019687	0.153950	10.31280	13.23270
BCG1355	185.43028	0.329512	0.156650	8.38778	10.61470
BCG1383	185.24322	11.528934	0.261950	11.40520	13.99760
BCG1408	187.79463	11.786205	0.172850	11.27210	13.43390
BCG1520	187.29306	14.728700	0.275450	9.69912	12.29420
BCG1529	191.95320	10.648070	0.243050	10.15970	12.65270
BCG1574	185.60712	6.502490	0.102650	7.37734	9.44810
BCG1635	187.69004	9.170359	0.291650	6.05027	7.71484
BCG1684	186.82361	2.601625	0.229550	7.50154	9.51897
BCG1805	188.03874	13.302351	0.278150	8.07326	10.13060
BCG1934	183.24882	7.898145	0.132350	7.24300	9.11284
BCG1961	184.82473	11.279270	0.253850	9.85226	11.54580
BCG2196	192.43198	1.746452	0.207950	6.77548	8.75636
BCG2199	193.94356	1.980950	0.288950	7.68495	9.16246
BCG2255	190.47262	10.902658	0.113450	5.97685	7.83891
BCG2296	186.72384	12.365892	0.164750	8.30567	10.67860
BCG2322	182.88571	10.805757	0.229550	8.58161	10.37810
BCG2395	180.60957	10.562301	0.232250	8.10823	9.51045
BCG2410	192.83481	10.812324	0.121550	6.90917	8.73994
BCG2566	188.37254	8.835154	0.248450	8.20927	10.14310
BCG2801	183.64345	0.791082	0.240350	7.34158	8.89927
BCG2833	187.20573	8.314187	0.218750	7.47353	9.13566
BCG2907	183.38725	7.421361	0.148550	8.42181	10.39250
BCG3098	186.99976	13.942666	0.253850	5.43397	6.64345
BCG3137	181.02868	1.779234	0.243050	6.02762	7.36433
BCG3194	193.99197	9.706866	0.240350	5.82393	6.94385
BCG3299	187.46419	14.412767	0.288950	6.20903	7.80151
BCG3332	192.11267	12.143343	0.270050	6.84018	8.07318
BCG3571	180.92705	1.031848	0.259250	6.88905	8.58642
BCG3728	189.20382	8.853715	0.170150	6.51664	8.38270
BCG3786	188.77550	19.269088	0.237650	6.90189	8.42570
BCG3809	183.87004	1.840244	0.256550	6.56095	7.96016
BCG3858	180.26887	15.209924	0.108050	4.72527	5.94890
BCG4032	194.52230	5.328463	0.286250	4.46252	5.58348
BCG4048	181.62656	1.820709	0.288950	5.12966	6.41988
BCG4106	181.03875	13.664575	0.207950	6.80957	8.51718
BCG4120	189.24367	14.695208	0.264650	7.04354	8.58972
BCG4189	185.44575	7.806539	0.135050	5.56824	6.99704
BCG4259	185.50020	15.793529	0.216050	6.42034	7.65803
BCG4262	180.89012	11.101584	0.256550	4.67782	5.85087
BCG4264	181.29986	10.435014	0.253850	6.57431	8.10770
BCG4391	185.94397	16.155459	0.248450	6.41880	7.84344
BCG4674	183.69782	0.515216	0.202550	7.41103	9.13500
BCG4702	188.48709	8.626259	0.251150	5.73425	6.95224
BCG4810	180.86246	11.157377	0.221450	7.27635	8.66375
BCG4909	192.35491	6.410631	0.221450	6.31448	7.76555
BCG4919	189.03059	9.055363	0.167450	6.52211	7.90281

Table 2. continued.

ID	RA (deg)	DEC (deg)	phot. redshift	L_r ($10^{10} L_{\odot}$)	L_i ($10^{10} L_{\odot}$)
BCG4920	186.05064	0.952353	0.234950	5.47253	6.75675
BCG4944	180.48399	0.963729	0.248450	6.43689	7.74543
BCG5015	191.47499	7.553409	0.291650	5.74592	7.19943
BCG5041	190.96045	18.839278	0.218750	6.40927	8.00857
BCG5189	181.25473	19.452434	0.124250	5.43648	6.80868
BCG5232	183.95954	12.750903	0.270050	5.27181	6.30323
BCG5349	182.97490	14.776806	0.232250	6.20429	7.53018
BCG5498	183.74276	1.511291	0.256550	5.74283	7.31763
BCG5636	187.66913	12.054116	0.164750	5.76002	6.94934
BCG5642	188.13099	11.164277	0.243050	6.27071	7.69720
BCG5758	184.84480	8.970715	0.243050	4.83305	6.04076
BCG5853	182.78875	1.682428	0.297050	4.12629	5.28630
BCG5856	186.39116	12.172804	0.248450	5.06026	6.06908
BCG5866	183.08498	1.807876	0.194450	5.64366	7.02486
BCG5908	186.80342	16.047996	0.261950	5.97824	7.30549
BCG6008	189.06966	15.771247	0.291650	4.43643	5.54013
BCG6133	185.44925	14.908885	0.283550	5.48976	6.70849
BCG6141	187.77102	15.936589	0.194450	5.42412	6.74935
BCG6336	185.21890	7.849342	0.267350	5.03954	6.09250
BCG6351	189.01712	15.538132	0.294350	3.96554	4.90615
BCG6414	186.96172	2.068728	0.261950	5.48571	6.75390
BCG6449	180.62687	1.254594	0.251150	5.24591	6.16955
BCG6452	186.17128	12.068727	0.270050	5.55227	6.83217
BCG6511	180.94678	2.493501	0.172850	6.05021	7.64602
BCG6591	191.16931	19.349601	0.229550	5.66044	7.01136
BCG6606	182.98453	7.124765	0.126950	4.22374	5.20826
BCG6654	184.97435	12.334273	0.288950	4.88175	6.07951
BCG6824	185.47382	1.625496	0.264650	5.09193	6.16209
BCG6963	190.84401	8.995975	0.164750	5.69739	7.32116
BCG7149	186.85432	13.905348	0.253850	3.65459	4.38088
BCG7211	183.18881	12.913723	0.153950	5.43045	6.61262
BCG7356	181.11548	10.303635	0.245750	5.28908	6.28420
BCG7528	187.55171	3.589214	0.245750	4.58078	6.12171
BCG7607	182.93436	1.420465	0.197150	4.91499	5.98166
BCG7665	182.16092	1.830234	0.191750	4.42660	5.46550
BCG7815	183.92328	13.822793	0.151250	4.27156	5.36755
BCG7849	186.20971	13.577342	0.280850	3.96076	5.01503
BCG7925	193.24545	2.326676	0.283550	3.20654	4.08633
BCG7970	182.71734	15.926379	0.102650	3.02490	3.78739
BCG7990	185.79064	1.788596	0.105350	4.12858	5.08073
BCG7992	189.35950	10.500427	0.280850	4.21600	5.28712
BCG8059	182.72015	6.179033	0.129650	5.02624	6.49310
BCG8085	183.78902	14.118415	0.151250	4.34757	5.56477
BCG8201	185.11668	12.234106	0.248450	4.55776	5.72813
BCG8239	194.86198	11.227184	0.226850	4.67188	5.54014
BCG8300	187.65753	1.941365	0.259250	4.14686	5.16082
BCG8338	188.56378	11.032966	0.286250	3.86246	4.77362
BCG8395	191.32203	10.341499	0.175550	4.40601	5.47262
BCG8511	185.80565	14.537155	0.288950	3.10920	3.94280
BCG8535	185.40671	7.354512	0.140450	4.50455	5.50313
BCG8603	187.85982	0.142061	0.143150	4.54750	5.68057
BCG8617	181.14647	2.785905	0.156650	3.97773	5.01955
BCG8643	187.66631	11.950027	0.261950	5.05360	6.20237
BCG8658	186.51783	1.453034	0.234950	4.06681	5.07874
BCG8692	185.05873	14.349871	0.253850	4.38472	5.36476
BCG8767	181.78993	9.395620	0.272750	5.20825	6.77733
BCG8918	187.49202	13.846595	0.270050	4.16003	5.11062
BCG8934	183.67468	13.613577	0.148550	4.14031	5.14870
BCG9065	184.50070	6.582688	0.264650	3.96678	4.94711
BCG9088	181.19525	15.022918	0.145850	3.57690	4.38010
BCG9106	183.95896	0.724226	0.243050	4.10985	5.19465

Table 2. continued.

ID	RA (deg)	DEC (deg)	phot. redshift	L_r ($10^{10} L_\odot$)	L_i ($10^{10} L_\odot$)
BCG9130	183.79112	1.164337	0.272750	5.33444	6.41501
BCG9161	191.99719	8.624872	0.256550	3.76567	4.60629
BCG9375	188.01972	1.465264	0.240350	3.78301	4.68663
BCG9402	190.47755	16.107645	0.288950	4.12880	4.94586
BCG9419	187.17228	13.676487	0.256550	4.65006	5.57512
BCG9455	194.07920	18.619761	0.183650	4.18043	5.33622
BCG9478	188.50546	11.973708	0.178250	4.55322	5.92121
BCG9512	189.25606	7.631371	0.299750	3.55800	4.34681
BCG9514	186.97122	16.030243	0.283550	3.33753	4.15719
BCG9686	186.11951	2.465236	0.207950	4.63002	5.94480
BCG9693	186.04074	8.730912	0.167450	3.74240	4.74735
BCG9737	184.80382	14.395416	0.259250	4.47137	5.52323
BCG9799	193.64689	10.002305	0.191750	3.62893	4.58484
BCG10141	185.55197	14.590736	0.224150	3.88453	4.72299
BCG10151	193.53080	3.804609	0.224150	3.64730	4.39979
BCG10217	194.28821	14.722016	0.221450	3.98609	4.88795
BCG10326	191.03480	8.069578	0.164750	3.84886	4.77938
BCG10339	183.42129	1.628454	0.234950	4.38894	5.31973
BCG10372	187.08285	14.608728	0.286250	2.72270	3.44370
BCG10430	180.91580	1.204584	0.102650	2.99825	3.73585
BCG10452	192.03184	11.352027	0.256550	3.62367	4.52326
BCG10815	192.97780	11.842069	0.175550	4.07066	5.10382
BCG11017	185.16711	1.404918	0.172850	3.62870	4.53496
BCG11239	188.99457	13.207563	0.170150	3.04897	3.80921
BCG11241	189.62273	5.904392	0.240350	3.41960	4.25677
BCG11369	189.41545	7.794008	0.178250	3.78488	4.57201
BCG11442	186.81470	9.169160	0.275450	3.32945	4.23054
BCG11482	180.85448	10.811054	0.210650	3.73503	4.63222
BCG11484	185.86695	15.655224	0.286250	2.89435	3.63280
BCG11518	189.07718	15.494217	0.256550	3.53120	4.22659
BCG11534	183.49782	1.602452	0.207950	3.29541	4.02701
BCG11547	187.59676	14.259085	0.256550	3.39592	4.05598
BCG11551	192.94604	3.879207	0.205250	3.80870	4.80651
BCG11571	187.65542	9.283149	0.240350	3.26598	4.09370
BCG11683	187.13218	2.635468	0.213350	3.38850	4.19167
BCG11703	187.70206	2.218458	0.248450	4.11068	5.11039
BCG11762	182.74433	1.192858	0.275450	3.50309	4.27821
BCG11787	187.53217	2.836198	0.137750	3.34340	4.21592
BCG11965	187.10510	13.898171	0.229550	2.88396	3.54409
BCG12016	186.49359	16.200333	0.221450	2.73968	3.33520
BCG12019	186.24668	11.836638	0.102650	2.16607	2.74446
BCG12122	188.76065	15.269065	0.245750	2.48031	2.99305
BCG12155	180.76919	10.410552	0.232250	2.92582	3.67983
BCG12463	185.14656	6.376248	0.118850	2.53692	3.09705
BCG12522	185.62052	14.471922	0.234950	2.33325	2.75455
BCG12632	182.74434	1.612938	0.297050	3.12973	3.70466
BCG12703	184.97424	7.512982	0.280850	2.18398	2.71403
BCG12990	192.18827	1.647833	0.183650	2.89727	3.58857
BCG13101	189.35622	10.383818	0.264650	2.53288	3.13100
BCG13175	193.80410	10.232985	0.164750	2.35196	2.94989
BCG13480	187.03828	8.954130	0.229550	1.90207	2.18253
BCG13497	188.38020	0.190788	0.183650	1.92044	2.40199
BCG13609	189.60870	15.768887	0.226850	1.95320	2.37338
BCG13639	192.86621	2.883622	0.218750	1.92269	2.40750
BCG13672	180.13584	0.336242	0.253850	1.52157	1.85562
BCG13790	185.21390	11.476087	0.229550	1.16904	1.43750

Table 3. Galaxies in our sample with spectroscopic information provided by SDSS: redshift, sub-class (AGN, STARFORMING, or BROADLINE), Mg2 and H β Lick indices and their uncertainty.

ID	spec. redshift	sub-class	Mg2	\pm	H β	\pm
BCG24	0.230558		0.313916	0.024135	1.624143	0.842013
BCG129	0.252744		0.254789	0.018935	0.947647	0.611584
BCG271	0.272047		0.274995	0.017862	2.101470	0.584695
BCG304	0.248118		0.293060	0.016535	1.441411	0.571690
BCG485	0.284612		0.272066	0.026296	1.362648	0.921333
BCG671	0.137062		0.288143	0.015167	2.183753	0.400882
BCG692	0.231012					
BCG933	0.225683		0.256044	0.019307	0.602522	0.693763
BCG1076	0.251505		0.276631	0.017347	2.785665	0.501516
BCG1123	0.113173		0.271697	0.009468	1.914185	0.278490
BCG1140	0.324538		0.221946	0.021216	1.258562	0.626185
BCG1152	0.144250		0.297741	0.011613	1.711954	0.344826
BCG1187	0.316567		0.285260	0.016848	1.749445	0.504575
BCG1251	0.146893		0.292536	0.014081	2.338836	0.493430
BCG1355	0.158895		0.280844	0.009324	1.602184	0.295529
BCG1383	0.254507		0.273814	0.016362	2.003437	0.512988
BCG1408	0.171116		0.301538	0.017347	1.501519	0.558158
BCG1520	0.285424		0.249108	0.021581	2.431830	0.765589
BCG1529	0.245753		0.262535	0.016176	1.070567	0.548029
BCG1574	0.075471	BROADLINE	0.278830	0.010293	1.364787	0.294204
BCG1635	0.321950		0.273304	0.023427	-0.048969	0.706194
BCG1684	0.218690		0.317027	0.012773	0.914725	0.590046
BCG1805	0.283662		0.252599	0.018863	0.840112	0.627715
BCG1934	0.137488		0.311870	0.010023	1.219293	0.280608
BCG1961	0.225744		0.264401	0.017479	1.400491	0.636460
BCG2196	0.201966		0.290880	0.020839	1.298720	0.715578
BCG2255	0.116928	BROADLINE				
BCG2296	0.163604		0.277711	0.016368	1.565580	0.522218
BCG2322	0.225985		0.285680	0.016465	1.087216	0.615393
BCG2395	0.229071		0.227800	0.016382	0.740022	0.596499
BCG2410	0.125230		0.290743	0.010008	1.168643	0.283420
BCG2566	0.251963		0.275614	0.020150	1.001811	0.694451
BCG2801	0.251029		0.261442	0.015082	0.970654	0.514771
BCG2833	0.214718		0.262154	0.022697	1.579777	1.061491
BCG2907	0.137207		0.239093	0.015403	1.684279	0.348206
BCG3137	0.240821		0.279896	0.018839	1.752254	0.681716
BCG3194	0.227791					
BCG3299	0.290972		0.280011	0.017548	1.264112	0.645362
BCG3332	0.263462		0.287693	0.022433	1.620180	0.707405
BCG3571	0.255169		0.241738	0.024016	2.952008	0.707217
BCG3728	0.165497		0.288372	0.016482	1.510066	0.529413
BCG3786	0.225821		0.270516	0.014891	1.181187	0.518753
BCG3809	0.241753		0.235692	0.019025	1.411908	0.689607
BCG3858	0.109187		0.311572	0.010663	1.377183	0.292759
BCG4032	0.324959		0.203827	0.030595	1.650039	0.828820
BCG4048	0.295877		0.261821	0.020166	2.665730	0.712405
BCG4106	0.205980		0.294526	0.016561	1.060984	0.675914
BCG4120	0.230859		0.254494	0.021146	1.600741	0.790321
BCG4189	0.137094		0.274778	0.014361	1.429085	0.397715
BCG4259	0.209841		0.271855	0.017336	2.728652	0.734529
BCG4262	0.288793		0.309794	0.029587	0.596318	1.027418
BCG4264	0.277109		0.268839	0.022987	1.420293	0.846605
BCG4391	0.233642		0.260215	0.027254	1.726228	1.030619
BCG4674	0.183824		0.265723	0.019309	0.534590	0.642284
BCG4702	0.250176		0.286761	0.016784	2.222454	0.548012
BCG4810	0.202245		0.290797	0.026173	2.369166	0.947302
BCG4909	0.225047		0.264383	0.017178	2.231198	0.752067
BCG4919	0.165049		0.295891	0.020710	1.875535	0.641725
BCG4920	0.235314		0.260306	0.022286	1.717322	0.848310
BCG4944	0.242670		0.255257	0.014690	2.228167	0.508443

Table 3. continued.

ID	spec. redshift	sub-class	Mg2	\pm	H β	\pm
BCG5015	0.285776		0.271097	0.023992	2.314066	0.813229
BCG5041	0.227974		0.266843	0.016595	1.377062	0.551542
BCG5189	0.132145	BROADLINE	0.286807	0.010781	1.367809	0.313986
BCG5232	0.264033		0.252630	0.021272	1.902738	0.689642
BCG5349	0.223418		0.214403	0.029562	2.294126	1.067352
BCG5498	0.242627		0.269739	0.021343	1.229566	0.783294
BCG5642	0.235521		0.260319	0.020424	3.442233	0.696234
BCG5758	0.255011		0.276979	0.026336	1.460787	0.903020
BCG5853	0.296180		0.287312	0.030376	1.137156	1.062628
BCG5856	0.254792		0.280112	0.021290	2.649512	0.642271
BCG5866	0.193292		0.274434	0.016210	1.366956	0.556039
BCG5908	0.231782		0.283237	0.020836	0.349850	0.789100
BCG6008	0.284115		0.327230	0.022497	1.443567	0.754465
BCG6133	0.296098		0.261117	0.023851	0.710391	0.838279
BCG6141	0.190765		0.279060	0.024338	2.091054	0.758165
BCG6336	0.268462		0.241370	0.021738	1.564736	0.736708
BCG6351	0.323224					
BCG6414	0.231156	STARFORMING	0.242674	0.017245	0.142032	0.657410
BCG6449	0.258681					
BCG6452	0.254429				2.003296	0.699393
BCG6511	0.164279		0.279094	0.013334	1.413066	0.426180
BCG6591	0.225377		0.224416	0.019607	2.907984	0.636684
BCG6606	0.135480		0.297471	0.012751	1.132342	0.343998
BCG6654	0.246205		0.199980	0.023050	1.667743	0.839960
BCG6824	0.267358		0.211951	0.024373	0.817268	0.777089
BCG6963	0.163213					
BCG7149	0.258033					
BCG7211	0.147835		0.271783	0.012884	2.711296	0.432613
BCG7356	0.237128		0.247838	0.022450	0.491749	0.860989
BCG7528	0.238646		0.254240	0.019507	2.450907	0.670883
BCG7607	0.185485		0.314032	0.018754	0.523212	0.619710
BCG7665	0.188359		0.250326	0.019063	1.907109	0.610453
BCG7815	0.156296		0.290713	0.016277	1.703787	0.488739
BCG7849	0.297713					
BCG7925	0.288204		0.319072	0.032785	1.828393	1.146880
BCG7990	0.110779		0.260042	0.010400	1.710873	0.299358
BCG7992	0.297880					
BCG8059	0.138473		0.238749	0.025068	0.793702	0.696294
BCG8085	0.157149		0.264521	0.020285	1.181411	0.645111
BCG8201	0.246665					
BCG8239	0.226726		0.231797	0.020208	2.718560	0.744617
BCG8300	0.268376					
BCG8338	0.297682					
BCG8395	0.182181		0.291955	0.014758	0.979427	0.477231
BCG8511	0.282993					
BCG8535	0.136322		0.249261	0.017110	1.604781	0.410299
BCG8603	0.134509		0.246746	0.018423	1.434693	0.441388
BCG8617	0.164692		0.273411	0.016561	1.824647	0.522287
BCG8643	0.247998					
BCG8658	0.260107					
BCG8692	0.258923					
BCG8767	0.284193					
BCG8918	0.266323					
BCG8934	0.157578		0.278197	0.018817	2.075243	0.562048
BCG9065	0.293149					
BCG9088	0.143465	AGN				
BCG9130	0.241417					
BCG9161	0.272666					
BCG9419	0.255641					
BCG9455	0.168573		0.227542	0.021991	2.536526	0.711398
BCG9478	0.151029		0.235051	0.016479	2.477687	0.594636

Table 3. continued.

ID	spec. redshift	sub-class	Mg2	\pm	H β	\pm
BCG9512	0.310271					
BCG9514	0.292013					
BCG9686	0.221717		0.284064	0.021264	2.206975	0.748415
BCG9693	0.176730		0.268354	0.018521	1.542066	0.608530
BCG9799	0.199863		0.257792	0.017475	0.461349	0.614137
BCG10141	0.225204		0.253260	0.022747	1.615399	0.890202
BCG10151	0.208103		0.246809	0.032352	2.047414	1.186051
BCG10217	0.224653		0.192641	0.018991	3.032758	0.647151
BCG10326	0.161365		0.275198	0.016163	1.633791	0.488293
BCG10339	0.221089		0.282606	0.023190	0.000000	-1.000000
BCG10372	0.284212					
BCG10430	0.077954		0.254954	0.014284	1.656597	0.381681
BCG10452	0.254391					
BCG10815	0.180769		0.246739	0.019481	0.005139	0.654559
BCG11017	0.159263		0.303790	0.018146	1.295591	0.555865
BCG11239	0.178699		0.224435	0.026502	1.138037	0.841920
BCG11369	0.176449		0.236906	0.016402	2.130898	0.570206
BCG11442	0.288675					
BCG11482	0.230001		0.195462	0.025990	2.273386	0.970192
BCG11547	0.255540					
BCG11551	0.219413		0.246214	0.029532	1.130792	1.433648
BCG11571	0.260091					
BCG11683	0.217616					
BCG11703	0.247557					
BCG11787	0.134161		0.261489	0.019548	1.456438	0.520110
BCG12019	0.100942		0.260534	0.015678	1.443693	0.437083
BCG12463	0.121134					
BCG12990	0.199584		0.242750	0.029549	1.733223	1.099187
BCG13175	0.153552		0.212377	0.019158	0.353287	0.683562

Table 4. UV photometry measurements (see Sect. 2.3).

ID	FUV exp.(s)	NUV exp.(s)	Aperture (pixels)	FUV (AB)	+1 σ	-1 σ	NUV (AB)	+1 σ	-1 σ	FUV-NUV center	+1 σ	-1 σ
BCG24	2315	3625	50	-17.50	0.23	0.29	-17.72	0.27	0.36	0.39	0.24	0.24
BCG129	1710	3060	30	-16.31	0.44	0.76	-16.58	0.35	0.52	0.55	0.71	0.87
BCG271	2568	5478	20	-16.20	0.32	0.46	-16.85	0.14	0.16	0.65	0.48	0.60
BCG304	1683	3101	30	-17.11	0.22	0.28	-17.53	0.17	0.21	0.03	0.27	0.27
BCG485	1746	4600	30	-17.15	0.22	0.28	-17.06	0.16	0.18	-0.42	0.30	0.31
BCG671	218	3457	50	-17.01	0.40	0.65	-17.39	0.15	0.18	-0.12	0.20	0.21
BCG692	4801	6313	30	-17.42	0.12	0.13	-17.78	0.11	0.12	0.14	0.18	0.18
BCG933	1295	1194	30	-16.41	0.28	0.37	-16.78	0.41	0.67	0.27	0.82	0.67
BCG1076	3469	8589	30	-16.81	0.21	0.26	-17.37	0.27	0.35	0.62	0.37	0.36
BCG1123	95	88	50	-15.02	1.87	114.92	-17.42	0.27	0.36	-0.22	0.37	0.39
BCG1140	1793	5063	30	-17.17	0.68	2.21	-17.64	0.52	1.02	0.78	1.52	4.28
BCG1152	3257	5934	50	-16.83	0.13	0.15	-17.13	0.11	0.13	0.12	0.10	0.10
BCG1187	15871	22264	30	-16.25	0.33	0.47	-17.37	0.12	0.14	0.88	0.30	0.34
BCG1251	210	3280	30	-17.12	0.19	0.23	-16.70	0.11	0.13	-0.44	0.22	0.24
BCG1355	185	219	30	-16.66	0.58	1.31	-17.66	0.18	0.22	0.67	0.48	0.61
BCG1383	5591	6627	30	-16.72	0.22	0.27	-16.91	0.20	0.24	0.23	0.31	0.31
BCG1408	5861	9594	30	-16.56	0.12	0.14	-18.07	0.04	0.04	1.43	0.11	0.12
BCG1520	4304	5187	30	-16.24	0.26	0.34	-17.07	0.25	0.33	0.75	0.36	0.36
BCG1529	3135	4743	30	-16.51	0.26	0.35	-17.29	0.18	0.21	1.00	0.41	0.47
BCG1574	110	1717	50	-16.71	0.39	0.61	-16.70	0.18	0.22	0.81	0.50	0.74
BCG1635	3306	5026	30	-17.33	0.25	0.32	-14.34	1.79	114.24	-1.98	114.92	1.07
BCG1684	29770	45512	30	-16.81	0.06	0.07	-17.06	0.09	0.10	0.02	0.11	0.10
BCG1805	2128	3681	30	-16.35	0.35	0.52	-18.41	0.16	0.19	3.98	1.24	113.85
BCG1934	1689	3106	50	-16.66	0.22	0.28	-17.22	0.15	0.18	0.83	0.18	0.19
BCG1961	1890	4689	20	-14.80	0.84	114.70	-16.34	0.20	0.25	1.54	1.09	114.90
BCG2196	1390	1264	20	-16.63	0.10	0.11	-16.65	0.11	0.12	0.01	0.22	0.22
BCG2199	2662	2413	20	-16.45	0.22	0.27	-16.28	0.32	0.46	-0.18	0.68	0.59

Table 4. continued.

ID	FUV exp.(s)	NUV exp.(s)	Aperture (pixels)	FUV (AB)	+1 σ	-1 σ	NUV (AB)	+1 σ	-1 σ	FUV-NUV center	+1 σ	-1 σ
BCG2255	1726	1638	50	-16.94	0.19	0.23	-16.68	0.29	0.40	-0.25	0.21	0.20
BCG2296	4780	4938	30	-16.39	0.11	0.12	-17.96	0.07	0.07	1.57	0.12	0.13
BCG2322	2296	3293	30	-16.02	0.40	0.64	-17.36	0.13	0.15	1.05	0.44	0.53
BCG2395	1295	1194	30	-16.92	0.30	0.41	-17.23	0.22	0.27	0.14	0.43	0.44
BCG2410	4274	7123	50	-16.80	0.11	0.12	-17.10	0.09	0.10	-0.14	0.07	0.07
BCG2566	5153	8371	20	-16.16	0.12	0.13	-16.65	0.09	0.10	0.48	0.21	0.22
BCG2801	3350	3288	30	-16.33	0.30	0.42	-16.81	0.23	0.29	0.09	0.43	0.43
BCG2833	1718	1578	20	-17.07	0.07	0.07	-17.03	0.11	0.12	-0.04	0.19	0.18
BCG2907	1682	2936	30	-15.91	0.15	0.17	-16.55	0.11	0.13	0.64	0.19	0.20
BCG3098	1651	3072	30	-16.24	0.57	1.26	-16.48	0.36	0.54	0.18	0.86	1.09
BCG3137	2334	2145	20	-16.23	0.19	0.23	-16.38	0.18	0.21	0.15	0.40	0.40
BCG3194	410	502	20	-99.90	0.00	-15.47	-2.99	1.27	102.89	-99.90	0.00	0.00
BCG3299	1651	1540	30	-99.90	0.00	-16.83	-17.25	0.28	0.38	1.43	1.70	115.16
BCG3332	3955	3582	30	-14.27	1.25	114.17	-16.32	0.29	0.40	0.46	0.61	0.70
BCG3571	3560	3264	20	-16.17	0.21	0.25	-15.72	0.28	0.38	-0.45	0.58	0.53
BCG3728	1764	1612	30	-15.94	0.21	0.26	-16.71	0.14	0.16	0.89	0.26	0.28
BCG3786	198	1583	30	-16.99	0.59	1.40	-16.61	0.76	116.51	-0.50	1.56	1.15
BCG3809	1801	1771	30	-16.43	0.78	116.33	-15.66	1.46	115.56	-3.02	114.04	2.62
BCG3858	108	165	30	-17.14	0.14	0.15	-16.71	0.23	0.29	-0.57	0.22	0.21
BCG4032	214	572	30	-17.15	1.02	117.05	-18.52	0.21	0.27	2.25	2.03	115.41
BCG4048	4721	5844	30	-16.55	0.44	0.76	-16.05	0.46	0.83	-0.66	0.69	0.65
BCG4106	133	122	30	-99.90	0.00	-16.77	-15.02	1.90	114.92	-1.05	115.36	117.08
BCG4120	5158	4780	30	-16.36	0.26	0.34	-16.79	0.22	0.27	0.24	0.31	0.31
BCG4189	1765	6045	30	-15.81	0.15	0.17	-17.25	0.05	0.06	1.01	0.12	0.12
BCG4259	6566	10217	30	-15.80	0.37	0.56	-16.62	0.20	0.24	0.79	0.43	0.49
BCG4262	1295	1194	30	-17.42	0.28	0.38	-16.98	0.40	0.64	-0.57	0.59	0.52
BCG4264	1381	1272	30	-18.20	0.09	0.10	-18.64	0.10	0.11	0.43	0.15	0.15
BCG4391	11095	12863	30	-16.32	0.18	0.22	-16.75	0.18	0.21	0.22	0.30	0.29
BCG4674	1675	1631	30	-17.03	0.16	0.19	-17.81	0.10	0.11	0.49	0.23	0.23
BCG4702	5153	8371	30	-17.80	0.05	0.06	-18.15	0.05	0.05	0.10	0.12	0.12
BCG4810	1295	1194	30	-15.72	0.46	0.80	-16.66	0.24	0.32	0.68	0.48	0.54
BCG4909	311	2004	30	-16.94	0.49	0.90	-16.91	0.31	0.43	0.16	0.66	0.85
BCG4919	2300	2118	30	-16.71	0.11	0.13	-16.83	0.12	0.14	0.14	0.17	0.17
BCG4920	1950	3431	30	-16.30	0.46	0.81	-16.81	0.24	0.31	0.69	0.62	0.83
BCG4944	1736	1593	30	-16.68	0.28	0.38	-16.66	0.35	0.52	-0.28	0.69	0.59
BCG5015	2339	2089	30	-15.69	0.83	115.59	-16.68	0.50	0.96	0.05	115.70	3.93
BCG5041	218	204	30	-17.50	0.32	0.45	-17.58	0.27	0.36	-0.03	0.47	0.48
BCG5189	108	101	30	-15.42	0.65	1.87	-17.13	0.20	0.25	1.46	0.81	1.39
BCG5232	1739	3997	20	-13.18	1.81	113.08	-15.46	0.25	0.33	2.28	2.14	113.33
BCG5349	211	1310	30	-99.90	0.00	-16.48	-16.44	0.38	0.58	-99.90	0.00	0.00
BCG5498	1675	1656	30	-16.58	0.33	0.48	-17.51	0.19	0.23	1.20	0.47	0.58
BCG5636	5382	9853	30	-16.09	0.15	0.17	-18.37	0.03	0.03	2.26	0.13	0.14
BCG5642	2135	5617	30	-15.23	0.86	115.13	-17.73	0.17	0.20	2.62	0.88	4.61
BCG5758	1594	3156	30	-16.19	0.39	0.61	-16.39	0.36	0.53	1.08	1.24	3.70
BCG5853	14920	15396	30	-15.63	0.42	0.70	-16.56	0.30	0.42	1.07	0.60	0.71
BCG5856	4100	4324	30	-16.10	0.31	0.43	-17.82	0.15	0.18	1.48	0.32	0.34
BCG5866	14663	14927	30	-15.91	0.13	0.15	-16.33	0.11	0.13	0.35	0.16	0.16
BCG5908	4607	4259	30	-16.53	0.25	0.33	-16.85	0.28	0.37	0.29	0.45	0.44
BCG6008	1746	3100	30	-16.76	0.49	0.92	-17.18	0.26	0.34	0.38	0.62	0.78
BCG6133	1660	3066	30	-15.96	0.81	115.86	-16.50	0.42	0.70	0.56	1.06	1.93
BCG6141	1352	2518	30	-16.56	0.31	0.44	-16.63	0.21	0.26	0.01	0.35	0.37
BCG6336	3338	7564	30	-99.90	0.00	-15.46	-15.90	0.38	0.60	3.23	2.80	112.41
BCG6351	1746	3100	30	-16.84	0.32	0.45	-17.14	0.38	0.60	-0.07	0.54	0.48
BCG6414	31310	46915	30	-16.83	0.07	0.08	-16.84	0.06	0.07	-0.23	0.12	0.12
BCG6449	1736	1593	30	-14.27	1.22	114.17	-15.87	0.64	1.74	0.04	4.77	1.75
BCG6452	4118	5785	30	-15.38	0.53	1.06	-17.45	0.20	0.24	1.60	0.40	0.46
BCG6511	2334	2145	30	-15.79	0.27	0.36	-16.66	0.15	0.17	0.62	0.26	0.28
BCG6591	108	101	30	-18.16	0.27	0.36	-18.51	0.22	0.28	0.34	0.50	0.53
BCG6606	1682	2936	50	-16.08	0.31	0.43	-16.71	0.16	0.19	0.66	0.19	0.21
BCG6654	1296	1195	30	-15.83	0.64	1.79	-17.10	0.28	0.37	1.01	0.88	1.30

Table 4. continued.

ID	FUV exp.(s)	NUV exp.(s)	Aperture (pixels)	FUV (AB)	+1 σ	-1 σ	NUV (AB)	+1 σ	-1 σ	FUV-NUV center	+1 σ	-1 σ
BCG6824	1842	1746	30	-16.41	0.50	0.97	-16.24	0.58	1.34	0.51	0.87	1.07
BCG6963	110	1624	30	-17.47	0.25	0.32	-17.99	0.06	0.06	0.01	0.15	0.16
BCG7149	1651	3072	30	-16.69	0.47	0.86	-16.23	0.44	0.76	-0.73	1.10	1.01
BCG7211	1635	3525	30	-15.92	0.19	0.24	-16.61	0.10	0.11	0.53	0.20	0.21
BCG7356	1381	1272	30	-16.91	0.31	0.44	-17.37	0.15	0.18	0.22	0.50	0.57
BCG7528	2668	5377	30	-15.48	0.79	115.38	-16.16	0.62	1.61	0.12	1.43	1.25
BCG7607	14920	15286	30	-16.93	0.04	0.04	-17.10	0.06	0.06	0.04	0.07	0.06
BCG7665	1770	3145	30	-16.00	0.35	0.51	-16.34	0.21	0.26	0.62	0.58	0.74
BCG7815	15872	23707	30	-16.43	0.05	0.05	-16.94	0.03	0.03	0.50	0.06	0.07
BCG7849	2150	3002	30	-15.46	1.06	115.36	-18.02	0.32	0.45	1.63	0.66	0.85
BCG7925	1340	1209	30	-16.15	0.59	1.36	-17.18	0.36	0.55	0.90	0.58	0.67
BCG7970	94	1642	30	-15.14	0.67	2.05	-16.09	0.13	0.15	2.69	1.65	112.84
BCG7990	1948	1843	50	-15.57	0.37	0.57	-16.62	0.19	0.24	1.18	0.29	0.32
BCG7992	1810	1721	30	-14.50	1.64	114.40	-14.94	1.36	114.84	3.36	118.28	112.21
BCG8059	101	3283	90	-18.77	0.36	0.55	-19.36	0.05	0.06	-0.09	0.08	0.08
BCG8085	15769	23611	90	-18.04	0.12	0.14	-18.73	0.07	0.07	0.76	0.06	0.06
BCG8201	1296	1195	30	-15.03	1.29	114.93	-16.61	0.44	0.76	-99.90	0.00	0.00
BCG8239	980	946	30	-16.17	0.55	1.16	-15.93	0.74	3.91	-0.39	1.01	0.80
BCG8300	32676	48586	30	-15.62	0.29	0.39	-16.27	0.21	0.26	0.58	0.39	0.41
BCG8338	1907	3329	30	-99.90	0.00	-15.70	-17.12	0.17	0.21	-99.90	0.00	0.00
BCG8395	1631	1508	30	-14.55	0.84	114.45	-15.66	0.57	1.28	0.71	1.18	1.31
BCG8511	1660	3066	30	-99.90	0.00	-16.13	-3.55	3.25	103.45	-9.64	105.65	113.89
BCG8535	4678	10217	30	-15.50	0.18	0.21	-16.13	0.09	0.10	0.83	0.24	0.26
BCG8603	4641	10557	30	-14.63	0.31	0.43	-16.23	0.07	0.07	1.89	0.38	0.51
BCG8617	2327	3604	30	-16.02	0.78	115.92	-16.41	0.18	0.22	0.13	0.74	1.40
BCG8643	4322	8475	30	-16.23	0.33	0.48	-17.85	0.16	0.19	1.53	0.38	0.43
BCG8658	10460	21304	30	-15.77	0.33	0.49	-16.56	0.15	0.18	0.93	0.47	0.59
BCG8692	19536	44877	30	-16.00	0.26	0.34	-16.84	0.08	0.09	0.43	0.23	0.26
BCG8767	91	85	30	-18.87	0.20	0.25	-18.34	0.30	0.42	-1.80	0.84	0.55
BCG8918	3350	3125	20	-14.92	0.54	1.13	-16.07	0.24	0.31	1.15	0.85	1.37
BCG8934	19040	29058	30	-15.65	0.12	0.13	-16.29	0.06	0.06	0.62	0.13	0.13
BCG9065	29950	30709	30	-15.88	0.24	0.31	-17.82	0.04	0.04	1.85	0.19	0.22
BCG9088	104	199	30	-16.62	0.41	0.66	-17.31	0.21	0.27	-0.13	0.45	0.45
BCG9106	1675	1631	30	-16.79	0.27	0.36	-17.79	0.14	0.16	0.82	0.24	0.26
BCG9130	1675	1656	30	-16.58	0.35	0.52	-16.52	0.63	1.65	0.65	1.00	0.97
BCG9161	2721	2579	30	-15.05	0.95	114.95	-16.44	0.37	0.57	-99.90	0.00	0.00
BCG9375	34739	52381	30	-16.83	0.08	0.08	-16.56	0.12	0.13	-0.35	0.14	0.14
BCG9402	2679	3950	30	-16.43	0.40	0.64	-16.13	0.57	1.29	0.57	0.93	1.11
BCG9419	6836	7256	30	-15.95	0.49	0.90	-17.15	0.34	0.50	1.68	0.70	0.96
BCG9455	201	313	30	-99.90	0.00	-15.96	-16.61	0.47	0.83	-99.90	0.00	0.00
BCG9478	6893	10114	30	-15.51	0.21	0.25	-16.85	0.10	0.10	1.45	0.23	0.25
BCG9512	3686	3548	30	-16.33	0.34	0.50	-15.66	0.79	115.56	-12.29	103.71	2.98
BCG9514	4607	5519	30	-17.02	0.21	0.26	-17.64	0.13	0.15	0.18	0.35	0.36
BCG9686	106	97	50	-19.51	0.23	0.29	-19.73	0.20	0.25	0.42	0.34	0.36
BCG9693	8434	7797	30	-16.15	0.14	0.16	-16.73	0.08	0.08	0.52	0.20	0.21
BCG9737	17977	44875	30	-15.51	0.53	1.09	-15.84	0.25	0.33	0.04	0.78	1.01
BCG9799	200	1667	30	-17.34	0.33	0.49	-17.41	0.12	0.14	1.30	0.82	2.82
BCG10141	1758	3157	30	-14.83	1.01	114.73	-16.43	0.29	0.39	0.27	0.75	0.87
BCG10151	1523	2991	30	-14.79	0.94	114.69	-16.27	0.36	0.54	1.96	1.46	113.89
BCG10217	203	252	30	-16.92	0.82	116.82	-18.49	0.17	0.20	1.50	0.73	1.54
BCG10326	1785	3263	30	-16.40	0.23	0.29	-17.30	0.08	0.09	0.55	0.20	0.22
BCG10339	14669	13644	30	-15.94	0.14	0.16	-16.33	0.21	0.27	0.24	0.39	0.35
BCG10372	4199	5089	30	-14.99	1.18	114.89	-14.13	1.78	114.03	-0.05	115.23	115.28
BCG10430	1736	1593	30	-14.33	0.36	0.54	-15.61	0.16	0.19	0.71	0.30	0.32
BCG10452	3244	3006	30	-15.90	0.43	0.72	-16.04	0.40	0.64	0.14	0.60	0.61
BCG10815	1726	3917	30	-13.91	1.34	113.81	-15.94	0.26	0.35	1.08	0.91	1.98
BCG11017	1937	1832	30	-14.19	1.00	114.09	-16.09	0.22	0.28	2.09	1.08	113.57
BCG11239	3469	8589	30	-15.21	0.35	0.53	-16.87	0.17	0.20	1.83	0.46	0.58
BCG11241	4216	8487	30	-15.93	0.52	1.05	-15.79	0.40	0.64	-0.43	0.67	0.69
BCG11369	1856	1783	30	-16.09	0.19	0.23	-16.93	0.19	0.23	0.56	0.37	0.36

Table 4. continued.

ID	FUV exp.(s)	NUV exp.(s)	Aperture (pixels)	FUV (AB)	+1 σ	-1 σ	NUV (AB)	+1 σ	-1 σ	FUV-NUV center	+1 σ	-1 σ
BCG11442	5227	6713	30	-16.88	0.18	0.21	-16.42	0.36	0.54	-0.24	0.37	0.33
BCG11482	1295	1194	30	-17.49	0.12	0.14	-18.54	0.08	0.08	1.13	0.14	0.15
BCG11484	6583	8691	30	-17.63	0.06	0.06	-17.60	0.14	0.16	-0.31	0.14	0.13
BCG11518	1746	1609	30	-16.73	0.32	0.47	-18.20	0.12	0.13	1.15	0.29	0.33
BCG11534	14669	13644	30	-15.70	0.18	0.21	-16.55	0.09	0.10	0.82	0.20	0.21
BCG11547	1651	1540	30	-99.90	0.00	-15.77	-16.75	0.36	0.53	-99.90	0.00	0.00
BCG11551	1523	1584	70	-19.51	0.25	0.32	-19.76	0.20	0.25	-0.12	0.18	0.18
BCG11571	3196	6403	30	-16.04	0.39	0.63	-16.83	0.16	0.19	1.00	0.46	0.60
BCG11683	29672	45423	50	-15.95	0.31	0.43	-16.80	0.17	0.20	0.91	0.22	0.24
BCG11703	32676	48586	30	-16.31	0.10	0.12	-17.03	0.05	0.05	0.55	0.09	0.10
BCG11762	14920	15286	30	-16.76	0.15	0.18	-17.47	0.08	0.09	0.79	0.21	0.22
BCG11787	29675	45494	50	-15.58	0.18	0.21	-16.13	0.08	0.08	0.45	0.11	0.11
BCG11965	3350	4658	30	-15.64	0.63	1.64	-15.81	0.36	0.53	-0.02	0.85	1.07
BCG12016	4617	4269	30	-15.92	0.26	0.34	-17.54	0.09	0.10	1.48	0.22	0.25
BCG12019	7934	9315	50	-15.62	0.24	0.31	-17.00	0.08	0.09	1.39	0.14	0.15
BCG12122	1769	3130	30	-15.86	0.52	1.05	-15.56	0.52	1.02	-0.21	0.70	0.72
BCG12155	1406	1296	30	-16.91	0.32	0.46	-17.12	0.21	0.26	0.24	0.53	0.60
BCG12463	29943	32240	50	-15.28	0.17	0.20	-16.23	0.07	0.08	0.85	0.10	0.10
BCG12522	1657	4605	30	-99.90	0.00	-15.41	-16.40	0.32	0.46	1.39	1.44	114.35
BCG12632	14920	15286	30	-15.90	0.32	0.45	-16.68	0.20	0.25	0.34	0.40	0.40
BCG12703	3232	7435	30	-16.57	0.24	0.31	-16.67	0.23	0.29	0.15	0.43	0.44
BCG12990	1390	1264	50	-18.56	0.13	0.15	-18.92	0.09	0.09	0.34	0.08	0.08
BCG13101	1810	1721	30	-99.90	0.00	-15.21	-16.56	0.45	0.78	-0.16	115.23	1.60
BCG13175	166	1756	30	-16.00	0.46	0.82	-16.85	0.13	0.14	1.45	0.65	1.26
BCG13480	4801	6313	30	-15.54	0.43	0.72	-18.34	0.04	0.05	3.34	0.53	0.98
BCG13497	4641	10557	30	-13.89	0.97	113.79	-15.45	0.29	0.40	1.81	1.20	113.21
BCG13609	1746	3064	30	-15.77	0.51	1.00	-16.13	0.44	0.75	-0.51	0.91	0.72
BCG13639	1340	1209	30	-14.08	1.72	113.98	-15.40	0.92	115.30	2.48	2.69	113.39
BCG13672	1858	1711	30	-17.42	0.16	0.19	-16.49	0.53	1.08	-1.37	1.08	0.62
BCG13790	5591	6627	30	-14.81	0.64	1.79	-15.23	0.61	1.49	-0.05	2.03	1.45

Table 5. Flags and notes for galaxies in our sample (see Sect. 2.5).

ID	Flag FUV	Flag NUV	Note
BCG24	ok	ok	
BCG129	ok	ok	
BCG271	part.	part.	
BCG304	ok	ok	
BCG485	ok	ok	
BCG671	ok	ok	
BCG692	ok	ok	Arcs
BCG933	ok	ok	
BCG1076	ok	ok	
BCG1123	ok	ok	
BCG1140	ok	ok	
BCG1152	ok	ok	
BCG1187	contam.	contam.	
BCG1251	ok	ok	
BCG1355	ok	ok	
BCG1383	ok	ok	Arcs
BCG1408	contam.	contam.	
BCG1520	ok	ok	
BCG1529	contam.	contam.	
BCG1574	ok	ok	shells/tails/asymmetric/mergers
BCG1635	ok	ok	shells/tails/asymmetric/mergers
BCG1684	ok	ok	
BCG1805	ok	ok	
BCG1934	ok	ok	
BCG1961	contam.	contam.	
BCG2196	contam.	contam.	

Table 5. continued.

ID	Flag FUV	Flag NUV	Note
BCG2199	contam.	contam.	
BCG2255	ok	ok	
BCG2296	ok	ok	
BCG2322	contam.	contam.	
BCG2395	contam.	contam.	
BCG2410	ok	ok	
BCG2566	contam.	contam.	
BCG2801	ok	ok	
BCG2833	contam.	contam.	
BCG2907	ok	ok	
BCG3098	ok	ok	
BCG3137	part.	part.	
BCG3194	part.	part.	
BCG3299	ok	ok	
BCG3332	ok	ok	
BCG3571	contam.	contam.	
BCG3728	ok	ok	
BCG3786	ok	ok	
BCG3809	ok	ok	
BCG3858	ok	ok	
BCG4032	contam.	contam.	
BCG4048	ok	ok	
BCG4106	ok	ok	
BCG4120	ok	ok	
BCG4189	contam.	contam.	Arcs
BCG4259	ok	ok	
BCG4262	ok	ok	
BCG4264	contam.	contam.	
BCG4391	ok	ok	
BCG4674	contam.	contam.	
BCG4702	contam.	contam.	shells/tails/asymmetric/mergers
BCG4810	ok	ok	
BCG4909	ok	ok	
BCG4919	ok	ok	
BCG4920	ok	ok	
BCG4944	ok	ok	
BCG5015	ok	ok	
BCG5041	ok	ok	
BCG5189	ok	ok	shells/tails/asymmetric/mergers
BCG5232	part.	part.	
BCG5349	ok	ok	
BCG5498	ok	ok	
BCG5636	contam.	contam.	
BCG5642	ok	ok	
BCG5758	contam.	contam.	shells/tails/asymmetric/mergers
BCG5853	ok	ok	
BCG5856	ok	ok	
BCG5866	ok	ok	
BCG5908	ok	ok	
BCG6008	ok	ok	
BCG6133	ok	ok	
BCG6141	ok	ok	
BCG6336	ok	ok	
BCG6351	ok	ok	
BCG6414	contam.	contam.	
BCG6449	ok	ok	shells/tails/asymmetric/mergers
BCG6452	ok	ok	
BCG6511	ok	ok	
BCG6591	ok	ok	
BCG6606	ok	ok	
BCG6654	contam.	contam.	

Table 5. continued.

ID	Flag FUV	Flag NUV	Note
BCG6824	ok	ok	
BCG6963	contam.	contam.	
BCG7149	contam.	ok	
BCG7211	part.	part.	
BCG7356	contam.	contam.	
BCG7528	ok	ok	
BCG7607	ok	ok	
BCG7665	ok	ok	
BCG7815	contam.	contam.	
BCG7849	ok	ok	
BCG7925	ok	ok	
BCG7970	ok	ok	
BCG7990	ok	ok	
BCG7992	ok	ok	
BCG8059	ok	ok	Spiral structure
BCG8085	contam.	contam.	Spiral structure
BCG8201	contam.	contam.	
BCG8239	ok	ok	
BCG8300	ok	ok	
BCG8338	contam.	contam.	
BCG8395	ok	ok	
BCG8511	ok	ok	
BCG8535	ok	ok	shells/tails/asymmetric/mergers
BCG8603	contam.	contam.	
BCG8617	ok	ok	
BCG8643	contam.	contam.	
BCG8658	ok	ok	
BCG8692	contam.	contam.	
BCG8767	contam.	contam.	
BCG8918	part.	part.	
BCG8934	ok	ok	
BCG9065	contam.	contam.	shells/tails/asymmetric/mergers
BCG9088	contam.	contam.	
BCG9106	contam.	contam.	
BCG9130	ok	ok	
BCG9161	ok	ok	
BCG9375	ok	ok	
BCG9402	ok	ok	
BCG9419	ok	ok	Arcs
BCG9455	ok	ok	
BCG9478	contam.	contam.	
BCG9512	contam.	contam.	
BCG9514	contam.	contam.	
BCG9686	ok	ok	Spiral structure
BCG9693	contam.	contam.	
BCG9737	ok	ok	
BCG9799	contam.	contam.	
BCG10141	ok	ok	
BCG10151	ok	ok	
BCG10217	ok	ok	
BCG10326	ok	ok	shells/tails/asymmetric/mergers
BCG10339	contam.	contam.	shells/tails/asymmetric/mergers
BCG10372	ok	ok	
BCG10430	ok	ok	
BCG10452	ok	ok	
BCG10815	ok	ok	
BCG11017	ok	ok	
BCG11239	ok	ok	
BCG11241	ok	ok	
BCG11369	contam.	contam.	shells/tails/asymmetric/mergers
BCG11442	ok	ok	

Table 5. continued.

ID	Flag FUV	Flag NUV	Note
BCG11482	ok	ok	
BCG11484	ok	ok	
BCG11518	contam.	contam.	
BCG11534	contam.	contam.	
BCG11547	ok	ok	
BCG11551	contam.	contam.	shells/tails/asymmetric/mergers
BCG11571	ok	ok	
BCG11683	ok	ok	
BCG11703	ok	ok	
BCG11762	ok	ok	shells/tails/asymmetric/mergers
BCG11787	ok	ok	
BCG11965	ok	ok	
BCG12016	ok	contam.	
BCG12019	ok	ok	Spiral structure
BCG12122	ok	ok	
BCG12155	contam.	contam.	
BCG12463	ok	ok	
BCG12522	ok	ok	
BCG12632	ok	ok	
BCG12703	ok	ok	
BCG12990	ok	ok	Spiral structure
BCG13101	ok	ok	
BCG13175	ok	ok	
BCG13480	contam.	contam.	
BCG13497	ok	ok	
BCG13609	contam.	contam.	
BCG13639	ok	ok	
BCG13672	ok	ok	
BCG13790	ok	ok	